AFOSR-TR-96 97

0123

REPORT DOCUMENTATION PAGE

1. AGENCY USE ONLY (Leave blank)	2. REPORT DATE	3. REPORT TYPE AND DATES COVERED
	February, 1997	Technical Report (3/1/96-9/30/96)

4. TITLE AND SUBTITLE
Direct Numerical Simulation of Flow Transition in Compressible Boundary Layer Around Airfoils

5. FUNDING NUMBERS
F49620 - 96-1-0122

6. AUTHOR(S)
Chaoqun Liu, Zhining Liu
Wei zhao, Guohua Xiong

7. PERFORMING ORGANIZATION NAME(S) AND ADDRESS(ES)
Department of Mathematics and Statistics
Louisiana Tech University
P.O. Box 3189
Ruston, LA 71272

8. PERFORMING ORGANIZATION REPORT NUMBER

9. SPONSORING/MONITORING AGENCY NAME(S) AND ADDRESS(ES)
AIR FORCE OFFICE OF SCIENTIFIC RESEARCH NA
Directorate of Aerospace Science
Bolling AFB, DC, 20332-6448

10. SPONSORING/MONITORING AGENCY REPORT NUMBER
96-1-0122

11. SUPPLEMENTARY NOTES

12a. DISTRIBUTION/AVAILABILITY STATEMENT
APPROVED FOR PUBLIC RELEASE
DISTRIBUTION IS UNLIMITED

19970314 040

13. ABSTRACT *(Maximum 200 words)*

The three-dimensional development of flow transition in both subsonic and supersonic Joukowsky airfoil boundary layers are studied by direct numerical simulation (DNS). The numerical simulation is performed by a spatial approach. A full compressible Navier-Stokes system in curvilinear coordinates is employed so that we can simulate the transition around general geometric configurations. The numerical results agree very well with the linear stability theory (LST) at the linear growth stage for both primary and second modes in the flat plate boundary layers. The whole process of controlled flow transition induced by blowing/suction around airfoils is simulated by directly solving the N-S system with Reynolds number around 10^6. Some differences are found in comparison to the incompressible counterpart, and some new phenomena for the transition around airfoils are observed which at least qualitatively agree with physics.

14. SUBJECT TERMS	15. NUMBER OF PAGES
Direct Numerical Simulation; Transition; Compressible; Three-dimensional; Airfoil; Navier-Stokes	42
	16. PRICE CODE

17. SECURITY CLASSIFICATION OF REPORT	18. SECURITY CLASSIFICATION OF THIS PAGE	19. SECURITY CLASSIFICATION OF ABSTRACT	20. LIMITATION OF ABSTRACT
Unclassified	Unclassified	Unclassified	

NSN 7540-01-280-5500

Standard Form 298 (Rev. 2-89)
Prescribed by ANSI Std. Z39-18
298-102

☆U.S. GOVERNMENT PRINTING OFFICE: 1994 - 528-064/23021

Direct Numerical Simulation of Flow Transition in Compressible Boundary Layer Around Airfoils

Chaoqun Liu, Zhining Liu, Wei Zhao, and Guohua Xiong
Numerical Simulation Group
Department of Mathematics and Statistics
Louisiana Tech University
P.O. Box 3189
Ruston, LA 71272

Abstract

The three-dimensional development of flow transition in both subsonic and supersonic Joukowsky airfoil boundary layers are studied by direct numerical simulation (DNS). The numerical simulation is performed by a spatial approach. A full compressible Navier-Stokes system in curvilinear coordinates is employed so that we can simulate the transition around general geometric configurations. The numerical results agree very well with the linear stability theory (LST) at the linear growth stage for both primary and second modes in the flat plate boundary layers. The whole process of controlled flow transition induced by blowing/suction around airfoils is simulated by directly solving the N-S system with Reynolds number around 10^6. Some differences are found in comparison to the incompressible counterpart, and some new phenomena for the transition around airfoils are observed which at least qualitatively agree with physics.

Contents

Direct Numerical Simulation of Flow Transition in Compressible Boundary Layer Around Airfoils

Chaoqun Liu, Zhining Liu, Wei Zhao, and Guohua Xiong
Numerical Simulation Group
Department of Mathematics and Statistics
Louisiana Tech University
P.O. Box 3189
Ruston, LA 71272

1 Introduction

In recent years, there has been a continuous and rapid improvement in understanding the process of transition from laminar to turbulent flow in incompressible boundary layers. Unlike the relatively comprehensive picture of transition scenarios in incompressible flows, nonlinear effects responsible for transition at high speeds are still very much a mystery (Erlebacher & Hussaini, 1990). In the absence of high-speed experimental data, direct numerical simulation (DNS) now plays an important role in understanding high-speed flow transition.

Several works on subsonic boundary layer transition have been published recently by other researchers (e.g., Fasel, 1990; Thumm et. al., 1990; Masad & Nayfeh, 1992; Masad & Iyer, 1993; Masad & Nayfeh, 1993). As the power of today's computer increases, direct numerical simulation (DNS) for realistic flow at certain Reynolds numbers becomes feasible. It is generally agreed that compressibility does not change the fundamental physics for streamwise instabilities at subsonic Mach number, but it still has many differences from incompressible instability, and the numerical simulation work is still very limited, especially for the complex geometries.

For supersonic flow transition, DNSs of flat-plate boundary layers over a wide range of Mach numbers (up to Mach 8 or higher) have resulted in some encouraging quantitative agreements (to several digits) with theories (Pruett et al, 1995). Several researchers have done great work on DNS for supersonic boundary layer transition (e.g., Erlebacher & Hussaini, 1990; Pruett & Zang, 1992; Eißler & Bestek, 1993; Fasel et al, 1993; Pruett et al, 1995; Adams & Kleiser, 1996; Guo et al; 1996). However, the high-speed transition

is very sensitive to subtle changes in inflow disturbances and basic state flow as well. The numerical simulation even for controlled transition in general geometries, such as airfoils, still remains a grand challenge up to date.

An alternative approach for studying flow transition is the PSE (parabolized stability equation) method (Herbert & Bertolotti, 1987; Bertolotti, 1991). This approach overcomes some severe limitations of the traditional linear stability theory (LST) by accounting not only for streamwise variations but also for inhomogeneous and nonlinear terms. Unfortunately, the cost of PSE increases much faster than that of DNS as the number of spanwise modes is increased. PSE thus is limited in practice to investigations of narrow-band forcing (Pruett et al, 1995). Furthermore, the parabolization limits information about downstream feedback, which is physically inaccurate. Other methods, like compressible linear stability theory (LST) (Mach, 1984) and secondary instability theory (SIT) (Ng & Erlebacher, 1992) can also provide limited information for flow transition, but are far away from practical application.

Therefore, in order to really solve the practical problems, an efficient and accurate solver for the full compressible time-dependent Navier-Stokes system must be developed. To date, Navier-Stokes codes fall roughly into two classes depending upon the application (Pruett et al.. 1995), *aerodynamic codes* which can handle complex geometry but are of low accuracy, and *DNS codes* which are of high accuracy but can only handle simple geometries. like channel, flat plate, and cone. Our goal is to develop a DNS code which is of high accuracy and can also handle complex geometry, so that we can simulate the real time-dependent compressible transitional and turbulent flow around aircraft components or subsystems, and eventually Air Force flight vehicles at all speeds.

Liu et al. (1996a,b) developed an approach which enables us to do the simulation of the whole process of transition in the incompressible boundary layers for airfoils. For the compressible flow, we can still adopt some of the techniques from our previous work. Though the implicit schemes have better numerical stability, they consume much more computer resources than explicit schemes, especially for complex geometry. For unsteady problems the time-step is very small, so that explicit schemes can also work well. In addition, explicit code is easy to vectorize and parallelize. In this study, we use explicit methods.

For subsonic transition cases, an explicit time-steeping code is generated using a sixth-

order central difference for the convection terms, a fourth-order central difference for the viscous terms, and a four stage fourth-order Runge-Kutta method for time integration. Under this frame, the CFL number can be increased to around 2.8, so that the time-step size for numerical stability is not too restricted. For supersonic transition cases, we generate our code for explicit time-stepping by adopting a sixth-order compact central difference (Lele, 1992) for both convection and diffusion terms, and a three-stage third-order compact Runge-Kutta method (Wray, 1986) for time integration.

The accuracy of the code is examined at the linear instability stage by comparing the numerical results with the linear stability theory (LST) at $M_\infty = 0.5$ and $M_\infty = 4.5$. The perturbation is introduced by wall suction/blowing upstream. After a certain distance of development, the least-stable mode is picked up and behaves the same as shown by LST. Two typical cases of the whole process of transition in the subsonic flat plate boundary layers, K-type and H-type breakdown, are calculated to ensure the robustness of the code. Transition over 2-D Joukowsky airfoils is then numerically simulated for both subsonic and low supersonic Mach numbers. Some new phenomena are observed.

2 Governing System

The 3-D, compressible, time-dependent Navier-Stokes equations are considered as the governing system in this work. On the general curvilinear coordinate system (ξ, η, ζ), these equations can be expressed as follows:

$$\frac{\partial \mathbf{U}}{\partial t} + \frac{\partial (\mathbf{E} - \mathbf{E}_v)}{\partial \xi} + \frac{\partial (\mathbf{F} - \mathbf{F}_v)}{\partial \eta} + \frac{\partial (\mathbf{G} - \mathbf{G}_v)}{\partial \zeta} = 0, \tag{1}$$

where

$$\mathbf{U} = \frac{1}{J}\begin{pmatrix} \rho \\ \rho u \\ \rho v \\ \rho w \\ e_t \end{pmatrix}, \quad \mathbf{E} = \frac{1}{J}\begin{pmatrix} \rho U \\ \rho U u + \xi_x p \\ \rho U v + \xi_y p \\ \rho U w + \xi_z p \\ (e_t + p) U \end{pmatrix},$$

$$\mathbf{F} = \frac{1}{J}\begin{pmatrix} \rho V \\ \rho V u + \eta_x p \\ \rho V v + \eta_y p \\ \rho V w + \eta_z p \\ (e_t + p) V \end{pmatrix}, \quad \mathbf{G} = \frac{1}{J}\begin{pmatrix} \rho W \\ \rho W u + \zeta_x p \\ \rho W v + \zeta_y p \\ \rho W w + \zeta_z p \\ (e_t + p) W \end{pmatrix},$$

$$
\begin{aligned}
\mathbf{E}_v &= \frac{1}{J}\begin{pmatrix} 0 \\ \xi_x\tau_{xx}+\xi_y\tau_{xy}+\xi_z\tau_{xz} \\ \xi_x\tau_{xy}+\xi_y\tau_{yy}+\xi_z\tau_{yz} \\ \xi_x\tau_{xz}+\xi_y\tau_{yz}+\xi_z\tau_{zz} \\ \xi_x(u\tau_{xx}+v\tau_{xy}+w\tau_{xz}-q_x) \\ +\xi_y(u\tau_{xy}+v\tau_{yy}+w\tau_{yz}-q_y) \\ +\xi_z(u\tau_{xz}+v\tau_{yz}+w\tau_{zz}-q_z) \end{pmatrix}, \\
\mathbf{F}_v &= \frac{1}{J}\begin{pmatrix} 0 \\ \eta_x\tau_{xx}+\eta_y\tau_{xy}+\eta_z\tau_{xz} \\ \eta_x\tau_{xy}+\eta_y\tau_{yy}+\eta_z\tau_{yz} \\ \eta_x\tau_{xz}+\eta_y\tau_{yz}+\eta_z\tau_{zz} \\ \eta_x(u\tau_{xx}+v\tau_{xy}+w\tau_{xz}-q_x) \\ +\eta_y(u\tau_{xy}+v\tau_{yy}+w\tau_{yz}-q_y) \\ +\eta_z(u\tau_{xz}+v\tau_{yz}+w\tau_{zz}-q_z) \end{pmatrix}, \\
\mathbf{G}_v &= \frac{1}{J}\begin{pmatrix} 0 \\ \zeta_x\tau_{xx}+\zeta_y\tau_{xy}+\zeta_z\tau_{xz} \\ \zeta_x\tau_{xy}+\zeta_y\tau_{yy}+\zeta_z\tau_{yz} \\ \zeta_x\tau_{xz}+\zeta_y\tau_{yz}+\zeta_z\tau_{zz} \\ \zeta_x(u\tau_{xx}+v\tau_{xy}+w\tau_{xz}-q_x) \\ +\zeta_y(u\tau_{xy}+v\tau_{yy}+w\tau_{yz}-q_y) \\ +\zeta_z(u\tau_{xz}+v\tau_{yz}+w\tau_{zz}-q_z) \end{pmatrix}, \\
e_t &= \frac{1}{2}\rho(u^2+v^2+w^2)+\frac{1}{\gamma-1}p, \\
\tau_{ij} &= \frac{\mu}{Re}(\frac{\partial u_i}{\partial x_j}+\frac{\partial u_j}{\partial x_i})-\delta_{ij}\frac{2}{3}\frac{\mu}{Re}\nabla\cdot\mathbf{V}, \\
q_i &= -\frac{\mu}{Re(\gamma-1)M_\infty^2 Pr}\frac{\partial T}{\partial x_i}, \\
T &= \gamma M_\infty^2\frac{p}{\rho}, \qquad (2)
\end{aligned}
$$

and

$$
\begin{aligned}
J &= \frac{\partial(\xi,\eta,\zeta)}{\partial(x,y,z)}, \\
U &= u\xi_x+v\xi_y+w\xi_z, \\
V &= u\eta_x+v\eta_y+w\eta_z, \\
W &= u\zeta_x+v\zeta_y+w\zeta_z.
\end{aligned}
$$

Here, $\mathbf{V}=(u,v,w)^T$. The four dimensionless parameters resulting from the nondimensionalization are defined as:

$$
M_\infty = \frac{U_\infty}{\sqrt{\gamma R_g T_\infty}},
$$

$$
\begin{aligned}
Re &= \frac{\rho_\infty U_\infty l^*}{\mu_\infty}, \\
Pr &= \frac{C_p \mu_\infty}{K_\infty}, \\
\gamma &= \frac{C_p}{C_v},
\end{aligned} \tag{3}
$$

where R_g, C_p, and C_v are the ideal gas constant and the specific heats at constant pressure and constant volume, respectively. Generally, we choose $Pr = 0.72$ and $\gamma = 1.4$ for subsonic and low Mach number supersonic flows. Viscosity is normalized by the viscosity at freestream, and is assumed to vary according to Sutherland's law. This yields

$$
\mu = T^{\frac{3}{2}} \frac{1+C}{C+T}, \quad C = 110.4K/T_\infty. \tag{4}
$$

The lengths are scaled by some reference length l^*. For the flat plate boundary layer flow, we use the boundary layer displacement thickness at the specified location, δ^*_{in}, where the disturbance is introduced. In general, with the dimensionless form, δ^* is defined as

$$
\delta^* = \int_0^\infty (1 - \rho u) dy. \tag{5}
$$

For the airfoil boundary layer flow, the half-thickness of the airfoil, h, is used as the reference length.

To reduce the machine's round-off error, we decompose the total flow into two parts: steady base flow and unsteady perturbation flow for the current work (in general, the base flow can also be unsteady flow). Assume

$$
\begin{aligned}
\mathbf{U} &= \mathbf{U}_0 + \mathbf{U}', \\
\mathbf{E} &= \mathbf{E}_0 + \mathbf{E}', \\
\mathbf{F} &= \mathbf{F}_0 + \mathbf{F}', \\
\mathbf{G} &= \mathbf{G}_0 + \mathbf{G}', \\
\mathbf{E}_v &= \mathbf{E}_{v0} + \mathbf{E}'_v, \\
\mathbf{F}_v &= \mathbf{F}_{v0} + \mathbf{F}'_v, \\
\mathbf{G}_v &= \mathbf{G}_{v0} + \mathbf{G}'_v,
\end{aligned}
$$

where the subscript "0" denotes the basic steady state flow, and prime ($'$) denotes the perturbation. The resulting governing system in the perturbation form is:

$$
\frac{\partial \mathbf{U}'}{\partial t} + \frac{\partial (\mathbf{E}' - \mathbf{E}'_v)}{\partial \xi} + \frac{\partial (\mathbf{F}' - \mathbf{F}'_v)}{\partial \eta} + \frac{\partial (\mathbf{G}' - \mathbf{G}'_v)}{\partial \zeta} = 0. \tag{6}
$$

In the above governing system, the vectors, the shear-stress tensor, and the heat-flux vector are given as follows:

$$\mathbf{U}' = \frac{1}{J}\begin{pmatrix} \rho' \\ (\rho u)' \\ (\rho v)' \\ (\rho w)' \\ e_t' \end{pmatrix},$$

$$\mathbf{E}' = \frac{1}{J}\begin{pmatrix} \rho_0 U' + \rho'(U_0 + U') \\ \rho_0 u_0 U' + (\rho u)'(U_0 + U') + \xi_x p' \\ \rho_0 v_0 U' + (\rho v)'(U_0 + U') + \xi_y p' \\ \rho_0 w_0 U' + (\rho w)'(U_0 + U') + \xi_z p' \\ (e_t' + p')(U_0 + U') + (e_{t_0} + p_0)U' \end{pmatrix},$$

$$\mathbf{F}' = \frac{1}{J}\begin{pmatrix} \rho_0 V' + \rho'(V_0 + V') \\ \rho_0 u_0 V' + (\rho u)'(V_0 + V') + \eta_x p' \\ \rho_0 v_0 V' + (\rho v)'(V_0 + V') + \eta_y p' \\ \rho_0 w_0 V' + (\rho w)'(V_0 + V') + \eta_z p' \\ (e_t' + p')(V_0 + V') + (e_{t_0} + p_0)V' \end{pmatrix},$$

$$\mathbf{G}' = \frac{1}{J}\begin{pmatrix} \rho_0 W' + \rho'(W_0 + W') \\ \rho_0 u_0 W' + (\rho u)'(W_0 + W') + \zeta_x p' \\ \rho_0 v_0 W' + (\rho v)'(W_0 + W') + \zeta_y p' \\ \rho_0 w_0 W' + (\rho w)'(W_0 + W') + \zeta_z p' \\ (e_t' + p')(W_0 + W') + (e_{t_0} + p_0)W' \end{pmatrix},$$

$$\mathbf{E}_v' = \frac{1}{J}\begin{pmatrix} 0 \\ \xi_x \tau_{xx}' + \xi_y \tau_{xy}' + \xi_z \tau_{xz}' \\ \xi_x \tau_{xy}' + \xi_y \tau_{yy}' + \xi_z \tau_{yz}' \\ \xi_x \tau_{xz}' + \xi_y \tau_{yz}' + \xi_z \tau_{zz}' \\ \xi_x[(u\tau_{xx})' + (v\tau_{xy})' + (w\tau_{xz})' - q_x'] \\ +\xi_y[(u\tau_{xy})' + (v\tau_{yy})' + (w\tau_{yz})' - q_y'] \\ +\xi_z[(u\tau_{xz})' + (v\tau_{yz})' + (w\tau_{zz})' - q_z'] \end{pmatrix},$$

$$\mathbf{F}_v' = \frac{1}{J}\begin{pmatrix} 0 \\ \eta_x \tau_{xx}' + \eta_y \tau_{xy}' + \eta_z \tau_{xz}' \\ \eta_x \tau_{xy}' + \eta_y \tau_{yy}' + \eta_z \tau_{yz}' \\ \eta_x \tau_{xz}' + \eta_y \tau_{yz}' + \eta_z \tau_{zz}' \\ \eta_x[(u\tau_{xx})' + (v\tau_{xy})' + (w\tau_{xz})' - q_x'] \\ +\eta_y[(u\tau_{xy})' + (v\tau_{yy})' + (w\tau_{yz})' - q_y'] \\ +\eta_z[(u\tau_{xz})' + (v\tau_{yz})' + (w\tau_{zz})' - q_z'] \end{pmatrix},$$

$$\mathbf{G}'_v = \frac{1}{J}\begin{pmatrix} 0 \\ \zeta_x\tau'_{xx}+\zeta_y\tau'_{xy}+\zeta_z\tau'_{xz} \\ \zeta_x\tau'_{xy}+\zeta_y\tau'_{yy}+\zeta_z\tau'_{yz} \\ \zeta_x\tau'_{xz}+\zeta_y\tau'_{yz}+\zeta_z\tau'_{zz} \\ \zeta_x[(u\tau_{xx})'+(v\tau_{xy})'+(w\tau_{xz})'-q'_x] \\ +\zeta_y[(u\tau_{xy})'+(v\tau_{yy})'+(w\tau_{yz})'-q'_y] \\ +\zeta_z[(u\tau_{xz})'+(v\tau_{yz})'+(w\tau_{zz})'-q'_z] \end{pmatrix},$$

and

$$\begin{aligned}
e'_t &= \frac{1}{2}\rho_0[(2u_0+u')u'+(2v_0+v')v'+(2w_0+w')w'] \\
&+ \frac{1}{2}\rho'[(u_0+u')^2+(v_0+v')^2+(w_0+w')^2]+\frac{1}{\gamma-1}p', \\
\tau'_{ij} &= \frac{\mu_0+\mu'}{Re}\bar{\tau}'_{ij}+\frac{\mu'}{Re}\bar{\tau}_{0_{ij}}, \\
q'_i &= -\frac{1}{Re(\gamma-1)M_\infty^2 Pr}[(\mu_0+\mu')\frac{\partial T'}{\partial x_i}+\mu'\frac{\partial T_0}{\partial x_i}], \\
(u_k\tau_{ij})' &= \frac{\mu_0+\mu'}{Re}[(u_{0_k}+u'_k)\bar{\tau}'_{ij}+u'_k\bar{\tau}_{0_{ij}}]+\frac{\mu'}{Re}u_{0_k}\bar{\tau}_{0_{ij}}, \\
\bar{\tau}'_{ij} &= (\frac{\partial u'_i}{\partial x_j}+\frac{\partial u'_j}{\partial x_i})-\frac{2}{3}\delta_{ij}\nabla\cdot\mathbf{V}', \\
\bar{\tau}_{0_{ij}} &= (\frac{\partial u_{0_i}}{\partial x_j}+\frac{\partial u_{0_j}}{\partial x_i})-\frac{2}{3}\delta_{ij}\nabla\cdot\mathbf{V}_0.
\end{aligned} \tag{7}$$

Again, the subscript "0" denotes the basic steady state flow, prime denotes the perturbation, $\mathbf{V}' = (u', v', w')^T$, and $\mathbf{V}_0 = (u_0, v_0, w_0)^T$.

With $\mathbf{U}'$ solved, the perturbation components can be retrieved from

$$\begin{aligned}
u' &= \frac{(\rho u)'-\rho' u_0}{\rho_0+\rho'}, \\
v' &= \frac{(\rho v)'-\rho' v_0}{\rho_0+\rho'}, \\
w' &= \frac{(\rho w)'-\rho' w_0}{\rho_0+\rho'}, \\
p' &= (\gamma-1)(e'_t-\frac{1}{2}q), \\
q &= \rho'[(u_0+u')^2+(v_0+v')^2+(w_0+w')^2] \\
&+ \rho_0[(2u_0+u')u'+(2v_0+v')v'+(2w_0+w')w'],
\end{aligned} \tag{8}$$

and T' is obtained from the state equation

$$T' = T_0(\frac{p'}{p_0}-\frac{\rho'}{\rho})\frac{\rho_0}{\rho_0+\rho'}. \tag{9}$$

3 Numerical Method

Because of the sensitivity of physics, DNS codes must meet the requirements of both high accuracy and strong numerical stability. Many high-order discretizations have been developed by other researchers, for example, spectral methods (Orszag, 1971), compact finite difference methods (Lele, 1992), upwind-biased differences (Rai & Moin, 1993), and standard high-order central differences. Because the boundary treatment for the compact difference scheme is sensitive, we use, for the subsonic cases, the standard sixth-order central difference for the convective terms, fourth-order central difference for the viscous terms. In the supersonic cases, we choose the sixth-order compact finite difference method (Lele, 1992) for both convection and diffusion terms.

For time-integration, most people use the so-called compact low-storage third-order Runge-Kutta scheme (Wray, 1986) for simulating the transition problem. This method is efficient for supersonic flow because with the same CFL number, the real time-step size in supersonic cases is relatively larger than in the subsonic situation. So in the supersonic cases, we adopt this method. For the subsonic cases, we adopt the classic four-stage fourth-order Runge-Kutta scheme with sixth-order central difference in space directions. By carefully rearranging the arrays in the code, we can arrange that this fourth-order Runge-Kutta scheme also has low storage.

We can rewrite the system into the semi-discrete form:

$$\frac{d}{dt}\mathbf{U}'_{i,j,k} + \mathbf{R}(\mathbf{U}'_{i,j,k}) = 0, \tag{10}$$

where $\mathbf{R}(\mathbf{U}'_{i,j,k})$ is the function defined by

$$\mathbf{R}(\mathbf{U}'_{i,j,k}) = [\boldsymbol{L}_C + \boldsymbol{L}_D]\mathbf{U}'_{i,j,k}, \tag{11}$$

where $\boldsymbol{L}_C$ and $\boldsymbol{L}_D$ are discretized operators for convection and diffusion, respectively. The fourth-order Runge-Kutta scheme used to solve a system of ODE corresponding to the discretized Navier-Stokes equations can be expressed as follows:

$$\begin{aligned}
\mathbf{U}'^{(0)} &= \mathbf{U}'^{(n)}, \\
\mathbf{U}'^{(1)} &= \mathbf{U}'^{(0)} - \frac{\Delta t}{2}\mathbf{R}^{(0)}, \\
\mathbf{U}'^{(2)} &= \mathbf{U}'^{(0)} - \frac{\Delta t}{2}\mathbf{R}^{(1)},
\end{aligned}$$

$$
\begin{aligned}
\mathbf{U}'^{(3)} &= \mathbf{U}'^{(0)} - \Delta t \mathbf{R}^{(2)}, \\
\mathbf{U}'^{(4)} &= \mathbf{U}'^{(0)} - \frac{\Delta t}{6}(\mathbf{R}^{(0)} + 2\mathbf{R}^{(1)} + 2\mathbf{R}^{(2)} + \mathbf{R}^{(3)}), \\
\mathbf{U}'^{(n+1)} &= \mathbf{U}'^{(4)}.
\end{aligned} \tag{12}
$$

Here, $\mathbf{R}^{(q)} = \mathbf{R}(\mathbf{U}'^{(q)})$, the superscript n denotes the time level at $n\Delta t$, and the mesh indices (i, j, k) associated with the solution vector $\mathbf{U}'$ and time step Δt are suppressed for convenience.

4 Boundary Conditions

The above system can be solved with proper specification of boundary conditions. In general, all flow quantities can be specified at the inflow boundary. The prescription of the inflow boundary conditions depends on the way that the disturbances are introduced into the base flow. We can use either LST or PSE to provide the eigenvectors at the inflow. However, we think a periodic blowing/suction at the wall is more natural.

Figure 1 gives a schematic description of the computational domain. Supposing the blowing/suction strip is located relatively far away from the inflow boundary, we can assume

$$
f'(x_0, y, z, t) = 0, \tag{13}
$$

where f' stands for the variables u', v', w', ρ', and p', respectively.

For the boundary conditions at the wall, we use no-slip and isothermal conditions:

$$
u'(x, y_{wall}, z, t) = w'(x, y_{wall}, z, t) = T'(x, y_{wall}, z, t) = 0. \tag{14}
$$

The wall normal velocity component is prescribed as a function of x, z, and t to generate the disturbances in the computational domain (Rist & Fasel, 1995):

$$
v'(x, y_{wall}, z, t) = \begin{cases} f'_v(x, z, t) & x \in [x_1, x_2], \\ 0 & x < x_1 \text{ or } x > x_2. \end{cases}
$$

In this work, we use

$$
\begin{aligned}
f'_v(x, z, t) &= \varepsilon_{2d} \sin\left(\frac{2\pi(x - x_1)}{(x_2 - x_1)}\right) \sin(\omega_{2d} t) \\
&+ \varepsilon_{3d} \sin\left(\frac{2\pi(x - x_1)}{(x_2 - x_1)}\right) \cos(\beta z) sin(\omega_{3d} t),
\end{aligned}
$$

where ε_{2d} and ε_{3d} are the amplitudes for 2D and 3D disturbances, respectively; β is the controlled spanwise wave number; and ω_{2d} and ω_{3d} are the frequencies for 2D and 3D disturbances. This disturbance represents a combination of one 2D wave and a pair of oblique waves.

In the spanwise direction, a periodic boundary condition is imposed.

In the far field, an exponential decay condition (Fasel et al, 1990) together with the sponge layer treatment (Collis & Lele, 1996) are employed to satisfy the non-reflection requirement. The exponential decay condition yields

$$f_{NJ} = f_{NJ-1} e^{-\gamma(y_{NJ}-y_{NJ-1})}. \tag{15}$$

Here,

$$\gamma = \frac{\sqrt{\alpha_R^2 + \beta}}{\sqrt{Re}},$$

where α_R is the real part of the streamwise wave number.

The sponge layers are also embedded in the inflow and outflow sections (see Figure 1) to eliminate the reflection in the streamwise direction. For subsonic flow, the inflow sponge is necessary, while for supersonic flow, the inflow sponge can be removed.

For the Runge-Kutta type method, the sponge is loaded at each single stage, thus, (12) needs to be modified by adding an exponentially decaying source term in space directions to the right hand side:

$$\frac{d}{dt}\mathbf{U}'(x,y,z) + \mathbf{R}(\mathbf{U}'(x,y,z)) = -f_d(x,y)\mathbf{U}'(x,y,z). \tag{16}$$

This artificial term generates a so-called stiff differential equation which needs to be treated implicitly. This yields:

$$\begin{aligned}
\mathbf{U}'^{(0)} &= \mathbf{U}'^{(n)}, \\
\mathbf{U}'^{(1)} &= [\mathbf{U}'^{(0)} - \frac{\Delta t}{2}\mathbf{R}^{(0)}]/[1 + \frac{\Delta t}{2}f_d(x,y)], \\
\mathbf{U}'^{(2)} &= [\mathbf{U}'^{(0)} - \frac{\Delta t}{2}\mathbf{R}^{(1)}]/[1 + \frac{\Delta t}{2}f_d(x,y)], \\
\mathbf{U}'^{(3)} &= [\mathbf{U}'^{(0)} - \Delta t\mathbf{R}^{(2)}]/[1 + \Delta t f_d(x,y)], \\
\mathbf{U}'^{(4)} &= [\mathbf{U}'^{(0)} - \frac{\Delta t}{6}(\mathbf{R}^{(0)} + 2\mathbf{R}^{(1)} + 2\mathbf{R}^{(2)} + \mathbf{R}^{(3)})]/[1 + \Delta t f_d(x,y)], \\
\mathbf{U}'^{(n+1)} &= \mathbf{U}'^{(4)}.
\end{aligned} \tag{17}$$

The sponge function is given by (see Figure 1 for the location)

$$f_d(x,y) = \begin{cases} f_{d1}(x,y) = A_{s1}(\frac{x_{s1}-x}{x_{s1}-x_0})^{N_{s1}} & x \in [x_0, x_{s1}), \quad y \in [0, y_s) \\ f_{d2}(x,y) = A_{s2}(\frac{x-x_{s2}}{x_{max}-x_{s2}})^{N_{s2}} & x \in (x_{s2}, x_{max}], \quad y \in [0, y_s) \\ f_{d3}(x,y) = A_{s3}(\frac{y-y_s}{y_{max}-y_s})^{N_{s3}} & x \in [x_{s1}, x_{s2}], \quad y \in (y_s, y_{max}] \\ f_{d4}(x,y) = A_{s1}(\frac{x_{s1}-x}{x_{s1}-x_0})^{N_{s1}} + A_{s3}(\frac{y-y_s}{y_{max}-y_s})^{N_{s3}} & x \in [x_0, x_{s1}), \quad y \in (y_s, y_{max}] \\ f_{d5}(x,y) = A_{s2}(\frac{x-x_{s2}}{x_{max}-x_{s2}})^{N_{s2}} + A_{s3}(\frac{y-y_s}{y_{max}-y_s})^{N_{s3}} & x \in (x_{s2}, x_{max}], \quad y \in (y_s, y_{max}] \\ 0 & \text{elsewhere} \end{cases} \tag{18}$$

Here, $A_{s1}, A_{s2}, A_{s3}, N_{s1}, N_{s2}$, and N_{s3} are prescribed constants. In this work, we choose $A_{s1} = A_{s2} = A_{s3} = 10$, and $N_{s1} = N_{s2} = N_{s3} = 3$.

5 Grid mapping

To assure that the numerical schemes of DNS have high accuracy, we need to make the accuracy of grid transformation schemes two orders higher than that of the flow scheme itself. In this paper, we only use a flat plate or a Joukowsky airfoil with zero attack angle as our investigation targets, so we are able to use analytical mapping to transfer the physical domain to the computational domain.

In subsonic and low supersonic Mach number flows, the primary mode dominates the transition process, while as Mach number goes to over $M_\infty = 3$, the second mode (Mach mode) becomes dominant. This requires use of different types of grid structure for the above two kinds of flows.

5.1 Grids for primary instability

For the problem of the flat plate boundary layer transition, the grid mapping function we used is

$$\eta(x,y) = \frac{\eta_{max} y(\sigma + y_{max})}{y_{max}(\sigma + y\sqrt{x_{in}/x})}\sqrt{\frac{x_{in}}{x}}. \tag{19}$$

Here, x_{in} is the location where Re^* is defined. Usually, we choose $x_{in} = x_2$ (see Figure 1). For the parallel base flow, the boundary layer thickness does not grow, so the above transformation becomes

$$\eta(y) = \frac{\eta_{max} y(\sigma + y_{max})}{y_{max}(\sigma + y)}. \tag{20}$$

A typical grid for 2D flat plate boundary layer transition is shown in Figure 2 (a). Note that we use straight lines (20) for $x < x_{in}$, and parabolas (19) for $x \geq x_{in}$. This avoided using too small time-steps required for the CFL condition.

5.2 Grids for second-mode instability

For high-speed ($M_\infty \geq 3$) flow transition, high gradients are usually concentrated near the wall and near the critical layer. With the aid of LST, we can estimate the location of critical layers, and then use an analytical mapping which clusters grid points in both wall and critical layer regions. For the flat plate with parallel base flow, we use the following mapping, which is similar to that used by Pruett et al. (1995).

1. In computational space:

$$\eta_j = (j-1), \qquad j = 1, 2, \cdots, NJ. \tag{21}$$

2. Map η to [-1,1]:

$$\bar{\eta}_j = \frac{\eta_j - \eta_{1/2}}{\eta_{1/2}} \tag{22}$$

where $\eta_{1/2} = \eta_{NJ}/2$.

3. There are five parameters for the mapping: $y_{max}, y_{1/2}, y_0, \Delta y$, and τ. As shown in Figure 2(b), the parameter y_{max} is the height of the computational domain; $y_{1/2}$ defines a point such that half of the total grid points lie between the wall and this point; y_0 is usually chosen near the critical layer, and Δy and τ are used to adjust the stretch strength near y_0. The next step maps [-1,1] onto itself but performs a clustering of grids about y_0;

$$\psi + \tau \tanh\left(\frac{\psi - \psi_0}{\Delta\psi}\right) = \frac{\bar{\eta} - \bar{\eta}_0}{\Delta\bar{\eta}}, \quad -1 \leq \bar{\eta} \leq 1. \tag{23}$$

4. Exponential transformation maps [-1,1] onto a physical interval $[0, y_{max}]$:

$$\begin{aligned} y(\psi) &= y_{max}\left(\frac{a^{(\psi+1)} - 1}{a^2 - 1}\right), \quad -1 \leq \psi \leq 1, \\ a &= \frac{y_{max} + \sqrt{y_{max}^2 - 4y_{1/2}(y_{max} - y_{1/2})}}{2y_{1/2}}. \end{aligned} \tag{24}$$

The remaining unknown quantities in (23) are determined as follows:

$$\begin{aligned} \psi_0 &= \log(1 + \frac{y_0}{y_{max}}(a^2 - 1))/\log(a) - 1, \\ \Delta\psi &= \Delta y_0/(dy/d\psi), \\ dy/d\psi &= \frac{y_{max}}{(a^2-1)} a^{(\psi_0+1)} \log(a). \end{aligned}$$

Equation (23) is solved by Newton's method to obtain ψ, and then (24) is used to obtain the grid coordinates in the physical interval $[0, y_{max}]$. For the nonparallel flat plate boundary layer, the local boundary thickness will be changed according to $\delta = \delta_{in}\sqrt{x/x_{in}}$, so we let

$$y = y_{in}\sqrt{x/x_{in}},$$

where y_{in} is the normal-direction coordinate we obtained above (at inflow). All the Jacobian metrics are obtained analytically.

5.3 Conformal Mapping for the Joukowsky Airfoil

For the airfoil boundary layer flow, we now restrict our problem to be zero-degree attack angle. For Joukowsky airfoils, conformal mapping is used to obtain the grids and transformation metrics analytically (Liu et al., 1996 a,b).

The grid generation process can be described as follows (Figure 3):

1. $(\xi, \eta) \Rightarrow (\xi_0, \eta_0)$:

$$\begin{aligned} \xi_0 &= \frac{1}{\sigma_A}\xi, \\ \eta_0 &= \eta\ . \end{aligned}$$

This step performs a uniform stretch in the streamwise direction so that the length of solid wall is $2a$. This implies

$$\sigma_A = \frac{\xi_t}{2a}.$$

2. $(\xi_0, \eta_0) \Rightarrow (\xi_1, \eta_1)$:

$$\begin{aligned} \xi_1 &= \frac{\sigma_B \xi_0}{\sigma_B + a - |\xi_0|} - a, \\ \eta_1 &= \frac{\sigma_C \eta_{1_{max}} \eta_0}{\sigma_C \eta_{max} + \eta_{1_{max}}(\eta_{max} - \eta_0)}. \end{aligned}$$

The first formula performs a clustering of grids about $\xi_1 = -a$, and the second one performs a clustering of grids about solid wall ($\eta_1 = 0$).

3. $(\xi_1, \eta_1) \Rightarrow (x_1, y_1)$:

By using the Joukowsky transformation

$$\begin{aligned} \xi_1 &= \frac{x_1}{2}(1 + \frac{a^2}{x_1^2 + y_1^2}), \\ \eta_1 &= \frac{y_1}{2}(1 - \frac{a^2}{x_1^2 + y_1^2}), \end{aligned}$$

we can evaluate x_1 and y_1.

4. $(x_1, y_1) \Rightarrow (x_2, y_2)$:

$$\begin{aligned} x_2 &= x_1 - \frac{k'a}{k'+1}, \\ y_2 &= y_1. \end{aligned}$$

This step performs a shift of y_1 axis in the streamwise direction.

5. $(x_2, y_2) \Rightarrow (x, y)$:

$$\begin{aligned} x &= \sigma_E x_2 (1 + \frac{a^2}{(k'+1)^2} \frac{1}{x_2^2 + y_2^2}), \\ y &= \sigma_E y_2 (1 - \frac{a^2}{(k'+1)^2} \frac{1}{x_2^2 + y_2^2}). \end{aligned}$$

This step will generate the grids we required. Here, $k' < 1$ is used to change the ratio of half-thickness/chord-length. For example, with $k' = 0.0116$, the ratio=1/16. Also, we use σ_E to normalize the airfoil and make the half-thickness equal to 1.

With the grid generated, we can also obtain the Jacobian metrics between the (ξ, η) plane and the (x, y) plane analytically.

6 Filtering

Because of the use of the central difference scheme, the two-point "saw-tooth" oscillations will generally be generated, especially in the low viscous region. Those oscillations can induce some spurious physical waves. To avoid this phenomenon, we can either put some scheme viscosity through the biased upwinding scheme (Rai & Moin, 1993), or through the two-step MacMormack-like dissipative method (Gottlieb & Turkel, 1976), or through explicit filtering. Due to the simplicity of explicit filtering, we adopt it in our code. A sixth-order filter is applied every 10 time-steps in the wall-normal direction, and every 20 steps in the streamwise direction for the subsonic cases. During the study of supersonic transition, we find that only the wall-normal direction filtering is necessary. A compact sixth-order filtering is used every 10 time-steps in that direction.

7 Intergrid dissipation

Current supercomputers are still far away from resolving all the length scales for fully developed turbulent flow, while the use of models to represent those unresolved scales can always cause the case-dependent problem. But, without using any model, most non-dissipative DNS schemes will blow up because of the lack of enough dissipative mechanism of the codes. The "intergrid dissipation" developed by Liu & Liu (1995) plays a positive role in our code. By using the difference of flow quantities between two grid levels, we are now able to eliminate those scales badly described by the current grid, and provide some dissipation caused by those subgrid scales.

A brief description is as follows. Suppose f^h is the quantity obtained on the global grid G^h. We first restrict it to the next coarse level grid G^{2h}, and then obtain the new value of $f^{h(new)}$ on the global grid G^h. However, if we simply adopt this $f^{h(new)}$, the effects of small scales will all be ignored. Therefore, a dynamic weight function, σ, is introduced to maintain the effect of small eddies. This yields

$$\begin{aligned} f^{h(new)} &= \sigma I_{2h}^{h} I_{h}^{2h} f^{h(old)} + (1-\sigma) f^{h(old)}, \\ \sigma &= \min\{2\kappa, 1\}, \\ \kappa &= \frac{1}{2}(\rho_0 + |\rho'|)(u'^2 + v'^2 + w'^2). \end{aligned}$$

Here, I_h^{2h} is a full-weighting restriction operator, and I_{2h}^{h} is a bi-linear interpolation operator.

For the detail of intergrid dissipation, see Liu & Liu (1995).

8 Computational Results and Discussion

8.1 Subsonic transition

8.1.1 Flat plate

The code is first validated for the Mach 0.5 flat plate boundary layer flows. The base flow is obtained by solving the compressible similarity system (Stewartson, 1964) using a shooting method. The solid is assumed to be adiabatic for the base flow and isothermal for the perturbation. The Reynolds number is set to $Re^* = 875$ (based on δ^*), and $\omega_{2d} = 0.1$. Compressible linear stability theory provides an eigenvalue $\alpha = 0.2636 - i0.005623$.

The whole computational domain is set to 15 T-S wavelengths to ensure the development of the least stable mode. The grid is 16/wave $\times 51 \times 1$, with the last wavelength used as

the buffer domain (sponge layer), and the stretch parameter in (19) is $\sigma = 2.5$. Also one T-S period is divided into 1000 time steps. The base flow is assumed to be parallel. Figure 4(a) depicts the disturbance amplitude of u' and v', showing that the least stable mode is picked up very well and grows as LST predicted. Also, we can see that the sponge layers successfully eliminate the reflecting waves in all directions to keep the physical domain very clean. Eigenfunctions of this case are also compared with LST and found to agree very well (Figure 4(b)).

Both K-type and H-type transitions in 2-D subsonic flat plate boundary layers are then simulated by using the same code.

For the K-type transition, we use a $193 \times 41 \times 32$ grid, which includes an inflow sponge (first 16 streamwise grid points), a suction/blowing slot (next 16 streamwise grid points), an outflow buffer domain (the last 16 streamwise grid points), and an approximately 9 T-S wavelengths physical domain. The stretch parameter in (19) is set to $\sigma = 2.5$. The Mach number is $M_\infty = 0.5$, and $T_\infty = 288K$. The height of the computational domain is 30 (based on the δ^* at the end point of suction/blowing slot, x_2). The amplitude of disturbance is set to $\varepsilon_{2d} = 0.02$, $\varepsilon_{3d} = 0.008$, the controlled spanwise wave number is $\beta = 0.2$, and the angular frequency $\omega = 0.1$. One forcing period is divided into 1000 time steps. It takes around 8 Cray C-90 CPU hours (one processor) to run the code for 10,000 time steps. As in our previous work, our DNS code can keep running without blowing up, and the process of breakdown is simulated up to the limit of current grid resolution. Figure 5 depicts the instantaneous contour plots of perturbation streamwise vorticity (ω_x) and spanwise vorticity (ω_z) on the $y^* = 0.18595,\ 0.48165,\ 0.85052$ (x, z) planes after 10 forcing periods. It shows that the transition process is very similar to that of incompressible flow, except that the "legs" of the so-called lambda waves are longer. Also, even after the lambda waves break into smaller scale eddies, the major splitting appears in the spanwise direction, while the length scale in the streamwise direction is relatively longer.

For the H-type transition, a $265 \times 45 \times 42$ grid is employed. In the streamwise direction, the whole domain is divided into a 16 point inflow sponge, a 24 point suction/blowing slot, a 24 point outflow buffer domain, and a physical domain. The stretch parameter is $\sigma = 2.2$. The Mach number is set to $M_\infty = 0.8$, and $T_\infty = 288K$. The height of the computational domain is 25 (based on the δ^* at the end point of suction/blowing slot). The amplitude of disturbance is set to $\varepsilon_{2d} = 0.012$, $\varepsilon_{3d} = 0.004$, the controlled spanwise wave number is

$\beta = 0.22$, and the angular frequency $\omega_{2d} = 0.15075$. One forcing period is divided into 550 time steps. It takes around 15 Cray C-90 CPU hours (one processor) to run the code for 12 forcing periods. Figure 6 shows the instantaneous contour plots of perturbation streamwise vorticity (ω_x) and spanwise vorticity (ω_z) on the $y^* = 0.1471,\ 0.3768,\ 0.6563$ (x, z) planes after 11 forcing periods. Basically, the transition process is very similar to that of incompressible flow, with staggered structure of the lambda waves at the secondary instability stage. Again, the "legs" of the lambda waves are relatively longer. One difference from the incompressible H-type transition is that the staggered lambda waves can only be observed in a very short regime for the compressible case. After that, the staggered structure is contaminated by the invading lambda waves from upstream, and a branching structure can be observed clearly from the vorticity contours. However, the structured pattern can be observed in a relatively long regime, so the compressibility has an overall effect of stabilizing the subharmonic modes, and makes the transition zone longer.

Since the perturbation is introduced through blowing/suction, many disturbance modes may coexist; this can cause our simulations to be more or less like the detuned type (Ng & Erlebacher, 1992).

8.1.2 Joukowsky airfoil

The first case here is the fundamental breakdown of a subsonic Joukowsky airfoil boundary layer transition. Note that now the reference length is the half-thickness of the airfoil, h. The parameters are set as follows:

$$
\begin{aligned}
M_\infty &= 0.5, \\
T_\infty &= 288K, \\
Re_h &= 4000 \quad (Re_L = 160,000), \\
Pr &= 0.72, \\
\omega &= 0.8, \\
\beta &= 1.3, \\
\varepsilon_{2d} &= 0.015, \\
\varepsilon_{3d} &= 0.01, \\
\sigma &= 0.25\ ,
\end{aligned}
$$

$$z \in [-\frac{\pi}{\beta}, \frac{\pi}{\beta}] .$$

The chordlength/half-thickness is 40, which makes the Reynolds number (based on the chordlength) $Re_L = 160,000$. A $281 \times 41 \times 31$ grid is employed. The wing is placed from streamwise grid point 41 to 261, and the blowing/suction slot is embedded between point 71 and point 79. The height of the computational domain is around $16h$, and the crest point of the airfoil is located at the position of 25% chordlength. Figure 7 gives a part of the grid for this case. For the time stepping, one forcing period is divided into 1200 time steps.

For the airfoil boundary layer transition, one major issue is that it contains both favorable and adverse pressure gradients in the streamwise direction. Before the disturbance reaches the crest point of the airfoil, the favorable pressure gradient will stabilize the flow, and thus the amplitude of disturbance is damped. After the disturbance has passed the crest point, the gradually increased adverse pressure gradient will destabilize the flow, and the amplitude of disturbance is expected to grow faster than that in the zero-pressure-gradient flat plate. This phenomenon can be observed clearly in the 2-D case. Figure 8 depicts the maximum perturbation rms amplitude in the computational domain. The parameters we used are the same as above, except $\epsilon_{2d} = 0.001, \epsilon_{3d} = 0$. Clearly, the perturbation damps much faster than that in the flat plate case, until it reaches the crest point of the airfoil. After that, a very strong amplification shows up. This can cause breakdown when 3-D disturbances are introduced.

Figure 9 gives the contour plots of perturbation u', v', w', p', ρ' for the above fundamental transition case. Similar to the flat plate boundary layer case, it first generates lambda waves; then the lambda waves break into smaller scale vortices, and cause the transition. One difference is that, in the present case, the perturbation u' has a relatively strong anisotropic structure (Figure 9 (a)). Till now, we have not found an answer to explain this phenomenon. Therefore, a more detailed investigation needs to be done later.

The final case studied for subsonic boundary layer transition for a 2-D airfoil is the subharmonic transition case. We have the following setups:

$$\begin{aligned} M_\infty &= 0.6, \\ Re_h &= 13400 \quad (Re_L = 670,000). \\ T_\infty &= 288.88K, \end{aligned}$$

$$
\begin{aligned}
Pr &= 0.72, \\
\omega_{2d} &= 1.206, \\
\omega_{3d} &= 0.603, \\
\beta &= 1.76, \\
\varepsilon_{2d} &= 0.01, \\
\varepsilon_{3d} &= 0.0075, \\
\sigma &= 0.15, \\
z &\in [-\frac{\pi}{\beta}, \frac{3\pi}{\beta}] .
\end{aligned}
$$

A 361 × 45 × 41 grid is used, in which the wing is located between the 41st and 321st streamwise grid point. The height of the computational domain is about 20 h, and the chordlength/half-thickness is 50. The blowing/suction slot is located between the 81st and 93rd grid points. For the time stepping, one forcing period (based on ω_{2d}) is divided into 1000 time steps. It takes around 25 Cray C-90 CPU hours (one processor) for our code to run for 11 forcing periods. The contour plots of perturbation u', v', w', p', ρ' for this case after 11 forcing periods are given in Figure 10. As mentioned by Ng & Erlebacher (1992), the subharmonic modes are the most unstable modes. This results in earlier onset of transition. In fact, the staggered structure of lambda waves is much weaker than that in the incompressible flow. Even after a relatively long distance, we can still find that u' and ρ' have large length scale in the streamwise direction, while the length scale in the spanwise direction becomes very small. This could cause a strong anisotropic structure for the turbulent flow around airfoils.

8.2 Supersonic transition

8.2.1 Code validation

The code for supersonic transition first is validated for the Mach 4.5 flat plate boundary layer flows. The base flow is obtained by solving the compressible similarity system (Stewartson, 1964) using a shooting method. The Reynolds number is set to $Re^* = 10,000$, $Pr = 0.7$, $T_\infty = 61.111$, and $\omega_{2d} = 2.0467$. The constant C in Sutherland's law is $C = 110.33$. Compressible linear stability theory provides an eigenvalue $\alpha = 2.248 - i0.0308$.

A 16/wave ×141 × 1 grid is used, with the last wavelength used as the buffer domain. Again, one T-S period is divided into 200 time steps. For blowing/suction case, Eiβler and

H. Bestek have shown that a second mode wave and an additional wave, which are called "multiple-viscous-solution", will be excited. Since the "viscous-solution" is weakly damped, the second mode becomes dominant due to its large amplification rate if the computation domain is long enough. We reach this goal by using the following approach: pick up all the eigenfunctions just before the buffer domain, using them as the inflow conditions, instead of using the blowing/suction to excite the perturbation for the next computation. Figure 11 depicts the disturbance amplitude of u' and v', showing that the least stable mode is picked up very well and grows almost the same as LST predicted. Though we still can observe a long wave in the amplitude curve, it is very weak.

A wall-normal distribution of the eigenfunctions for the Mach 4.5 second mode is also obtained and compared at $Re^* = 10,000$ in Figure 12. It can be observed that even with blowing/suction, our code can still pick up the least stable mode which matches the result obtained from LST very well.

8.2.2 Joukowsky airfoil

Though the second mode is dominant for high Mach numbers, the transition zone is relatively long. On the other hand, for low supersonic Mach number, the viscous first-mode disturbances are dominant in the linear and nonlinear stability stages. Two breakdowns at Mach 1.6 are simulated in this work: **fundamental breakdown** and **oblique breakdown**.

For the fundamental breakdown, we use the following parameters:

$$\begin{aligned} M_\infty &= 1.6, \\ Re_h &= 15,000, \\ T_\infty &= 300K, \\ Pr &= 0.72, \\ \omega_{2d} &= 0.75, \\ \beta &= 2.28, \\ \varepsilon_{2d} &= 0.02, \\ \varepsilon_{3d} &= 0.001, \\ \sigma &= 0.25, \\ z &\in [-\frac{\pi}{\beta}, \frac{\pi}{\beta}] . \end{aligned}$$

The estimated wave angle of the enforced disturbance is $\psi \approx 60°$. A $361 \times 71 \times 37$ grid is used, with the wing located between the 41st and 321st streamwise grid points. The height of the computational domain is about $23h$, and the chordlength/half-thickness is 60, which makes the Reynolds number (based on the chordlength) $Re_L = 900,000$. The blowing/suction slot is located between the 61st and 77th grid points. For the time stepping, one forcing period (based on ω_{2d}) is divided into 600 time steps. It takes around 25 CRAY-C90 CPU hours and 25 MW memory for our code to run 14 forcing periods.

Figure 13 depicts the instantaneous contour plots of u', v', w', p', and ρ' after 14 forcing periods. It can be seen that even though we imposed only a pair of very weak 3-D disturbances (5% the magnitude of 2-D's), those disturbances are very unstable (see Figure 13 (c) for spanwise component of perturbation velocity). The process of transition is still the same as that in subsonic flow: 2D and 3D disturbance development, generation of lambda waves, and high shear layer breakdown. Not as we expected in the low speed boundary layer flow, the spanwise velocity components can grow even in the favorable-pressure-gradient regime before the crest point of the wing, where the 2-D disturbances decrease in this regime. A quick breakdown occurs after the disturbances enter the adverse-pressure-gradient regime, and the disturbance quantities reach the saturated level very early. This property can be observed more clearly form Figure 14, in which we give the maximum rms value of the perturbation quantities in two selected (x, y) planes, $z = 0$ and $z = \frac{\pi}{2\beta}$. The quick growth of the disturbances appears, and after breakdown, the rms of disturbances keeps at a relatively stable level (saturated).

The instantaneous contour plots of the streamwise and spanwise perturbation vortices as well as the perturbation vorticity magnitude are also given in Figure 15, which provides a better understanding of the fundamental breakdown structure for the 2D airfoil in low supersonic Mach number.

Another case simulated in this work is the "oblique breakdown". For this case, the same parameters as for the simulation of fundamental breakdown are used, except for the following differences: At the blowing/suction slot, we impose only one pair of 3D disturbance waves with finite amplitude $\varepsilon_{3d} = 0.0075$, and with controlled spanwise wave number $\beta = 1.59$, making the estimated wave angle $\psi = 45°$.

As in the fundamental breakdown case, the 3D disturbances can grow in the favorable pressure gradient regime before they reach the crest point of the wing. This is different

from incompressible and subsonic flow transition. A quick breakdown occurs after the disturbances enter the adverse pressure-gradient regime. Figure 16 gives the maximum rms value of the perturbation quantities in two selected (x, y) planes, $z = 0$ and $z = \frac{\beta}{2\pi}$. Quick growth of the disturbances is observed. By comparing Figure 14 and Figure 16, we find that the disturbances in the oblique breakdown case increase faster than those in the fundamental case. The saturated level also appears earlier than in the fundamental breakdown case. Therefore, we can consider that the oblique breakdown is a major factor for boundary layer transition at low supersonic Mach number.

Figure 17 depicts the instantaneous contour plots of disturbance quantities, u', v', w', p', and ρ'. Obviously, the structure of 3D disturbance development is different from that of the fundamental case. No lambda wave is observed in this case. Instead, a "zig-zag" type of the vortices are observed, followed by a branching structure. The instantaneous contour plots of the streamwise and spanwise perturbation vortices as well as the perturbation vorticity magnitude are given in Figure 18, which provides a better understanding of the oblique breakdown structure for the 2D airfoil in low supersonic Mach number. It can also be found that two high-shear layers per wavelength in the spanwise direction appear, organized in the streamwise direction in a staggered pattern.

9 Concluding Remarks

In summary, the current approach shows the ability of DNS to simulate the whole process of flow transition around 2-D airfoils with medium Reynolds number ($\approx 10^6$) for both subsonic and low supersonic Mach numbers. It demonstrates that realistic numerical simulations of compressible transition phenomena based on the spatial approach are already feasible with current generation of supercomputers. Although the computational results agree well with LST and qualitatively agree well with theory and experiment, the code still needs to be further validated. Once validated, this simulation can be extended to explore new physical phenomena and may partially substitute for wind tunnel experiments, especially for high-speed flows.

10 Acknowledgment

The authors are grateful to AFOSR for support. The authors wish to thank DoD HPC for providing CRAY-C90 and SP2 time for this study.

References

[1] Adams, N.A. and Kleiser, L., Subharmonic transition to turbulence in a flat-plate boundary layer at Mach number 4.5. *J. Fluid Mech.*, Vol 317, pp.301-335, 1996.

[2] Bertolotti, F.P., *Linear and Nonlinear Stability of Boundary Layers with Streamwise Varying Properties*, Ph.D. thesis, The Ohio State University, Columbus, Ohio, 1991.

[3] Collis, S.S. and Lele, S.K., A computational approach to swept leading-edge receptivity. *AIAA* 96-0180, 1996.

[4] Eiβler, W. and Bestek, H., Spatial numerical simulations of nonlinear transition phenomena in supersonic boundary layers. *Transitional and Turbulent Compressible Flows* (L.D. Kral & T.A. Zang eds), FED-Vol.151, pp.69-76, ASME, 1993.

[5] Erlebacher, G. and Hussaini M.Y., Numerical experiments in supersonic boundary-layer stability, *Phys. Fluids* A **2(1)**, 1990

[6] Fasel, H. Numerical simulation of instability and transition in boundary layer flows. *Laminar-Turbulent Transition* (D. Arnal and R. Michel Eds), pp.587-598. Springer-Verlag, 1990.

[7] Fasel, H., Rist, U., and Konzelmann, U., Numerical investigation of the three-dimensional development in boundary-layer transition. *AIAA J.* Vol 28, No.1, pp.29-37, 1990.

[8] Fasel, H., Thumm, A., and Bestek, H., Direct numerical simulation of transition in supersonic boundary layers: oblique breakdown. *Transitional and Turbulent Compressible Flows* (L.D. Kral & T.A. Zang eds), FED-Vol.151, pp.77-92, ASME, 1993.

[9] Gottlieb, D. and Turkel, E. Dissipative two-four methods for time-dependent problems. *Math. Comput.* Vol 30, No.136, pp.703-723, 1976.

[10] Guo, Y., Kleiser, L., and Adams, N.A., Comparison of temporal and spatial direct numerical simulation of compressible boundary-layer transition. *AIAA J.*, Vol 34, No.4, pp.683-691, 1996.

[11] Herbert, Th. and Bertolotti, F.P., Stability analysis of nonparallel boundary layers. *Bull. Am. Phys. Soc.*, 32:2079, 1987.

[12] Lele. S.K., Compact finite difference schemes with spectral-like resolution, *J. Comput. Phys.* **103**, pp.16-42, 1992.

[13] Liu, C., and Liu, Z., Multigrid mapping and box relaxation for simulation of the whole process of flow transition in 3-D boundary layers, *J. Comput. Phys.*, **119**, pp.325-341, 1995.

[14] Liu, Z., Xiong, G., and Liu, C, Direct numerical simulation for the whole process of transition on 3-D airfoils, *AIAA* 96-2081, 1996a.

[15] Liu, Z., Xiong, G., and Liu, C., Leading edge receptivity to the freestream vortical disturbance of 2-D and 3-D airfoils, *AIAA* 96-2084, 1996b.

[16] Liu, Z., Zhao, W., Xiong, G., and Liu, C., Direct numerical simulation of flow transition in high-speed boundary layers around airfoils, *AIAA* 97-0753, 1997.

[17] Mach, L.M., Boundary-layer linear stability theory. In *Special Course on Stability and Transition of Laminar Flow* (R. Michel ed.). AGARD Report No. 709, pp.3.1-3.81, 1984.

[18] Masad, J.A. and Nayfeh, A.H., Effect of a bulge on the subharmonic instability of subsonic boundary layers. *J. AIAA* **Vol 30 No. 7**, 1992.

[19] Masad, J.A. and Iyer, V. *Transition Prediction and Control in Subsonic Flow Over a Hump*, **NASA CP-4543**, 1993.

[20] Masad, J.A. and Nayfeh, A.H., The influence of imperfections on the stability of subsonic boundary layers. *Instabilities and Turbulence in Engineering Flows* (D.E. Ashpis et al eds), pp.65-82. Kluwer Academic Publishers, 1993.

[21] Ng, L. and Erlebacher, G., Secondary instabilities in compressible boundary layers, *Phys. Fluids:A* Vol.4, No.4, pp.710-726, 1992.

[22] Orszag, S.A., Numerical simulation of incompressible flows within simple boundaries: accuracy. *J. Fluid Mech.* Vol 49, pt.1, pp.75-112, 1971.

[23] Pruett, C.D. and Zang, T.A., Direct numerical simulation of laminar breakdown in high-speed, axisymmetric boundary layer. *Theoret. Comput. Fluid Dynamics* **3**, pp.345-367, 1992.

[24] Pruett, C.D., Zang, T.A., Chang C.-L., Carpenter, M.H., Spatial direct numerical simulation of high-speed boundary-layer flows. 1. Algorithmic considerations and validation. *Theoretical and Computational Fluid Dynamics* **7** No.1, pp.49-76, 1995.

[25] Rai, M.M. and Moin, P. Direct simulations of transition and turbulence in a spatially evolving boundary layer. *J. Comput. Phys.* **109**, pp.169-192, 1993.

[26] Rist, U. and Fasel, H. Direct numerical simulation of controlled transition in a flat-plate boundary layer, *J. Fluid Mech.* Vol 298, pp.211-248, 1995

[27] Stewartson, K. *The Theory of Laminar Boundary Layers in Compressible Fluids.* Oxford Mathematical Monographs, Oxford University Press, 1964.

[28] Thumm, A., Wolz, W., and Fasel, H. Numerical simulation of spatially growing three-dimensional disturbance waves in compressible boundary layers. *Laminar-Turbulent Transition* (D. Arnal and R. Michel Eds), pp.303-308. Springer-Verlag, 1990.

[29] Wray, A.A. Very low storage time-advancement schemes. *Internal Report*, NASA-Ames Research Center, Moffet Field, CA, 1986.

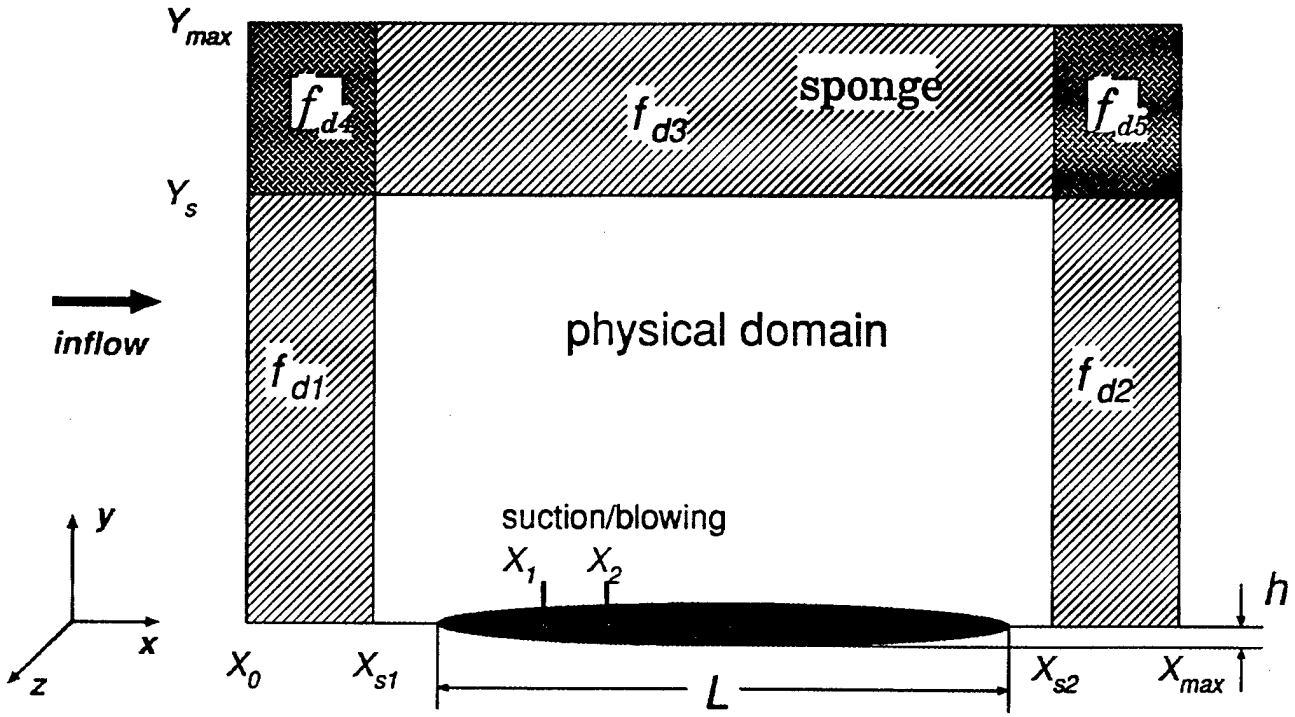

Figure 1. Sketch of the computational domain of a 2D airfoil with zero attack angle.

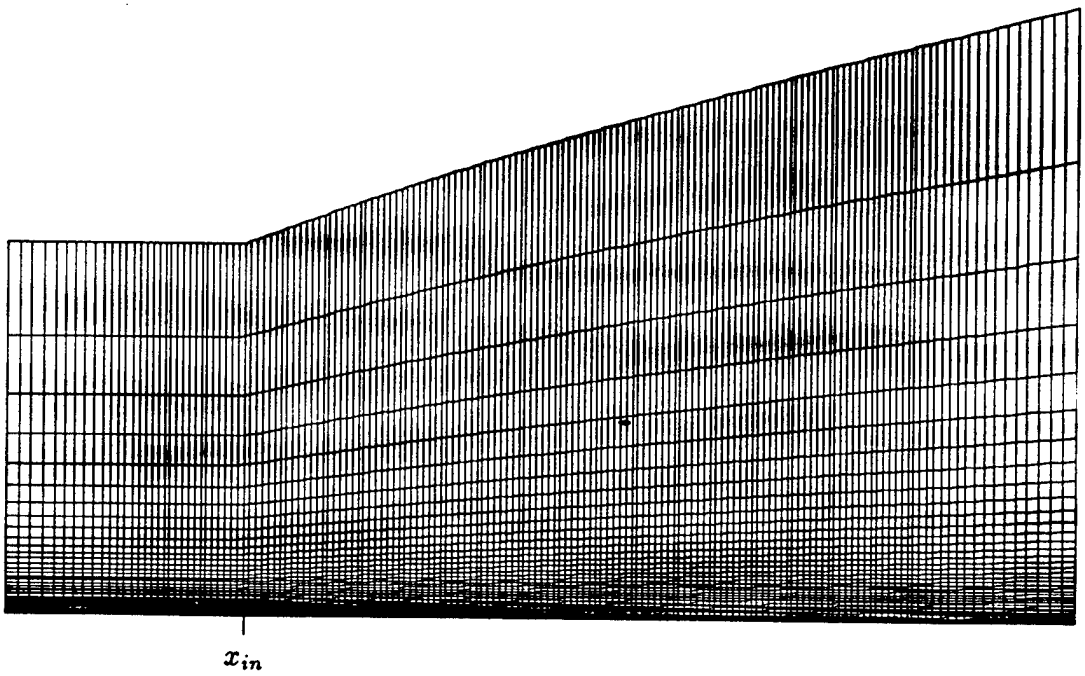

Figure 2 (a). A typical 2D grid for simulating flat plate boundary layer transition (primary mode).

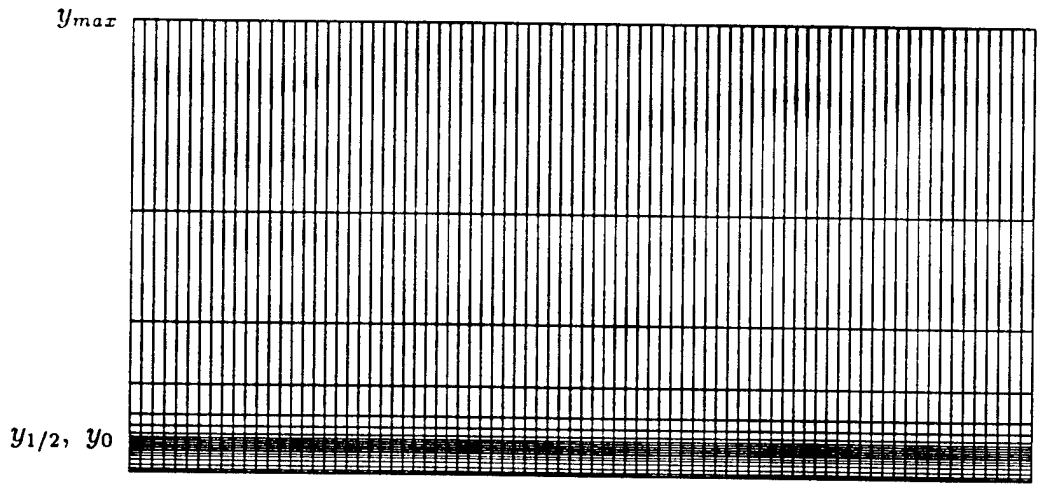

Figure 2 (b). A typical 2D grid for simulating flat plate boundary layer transition (second mode).

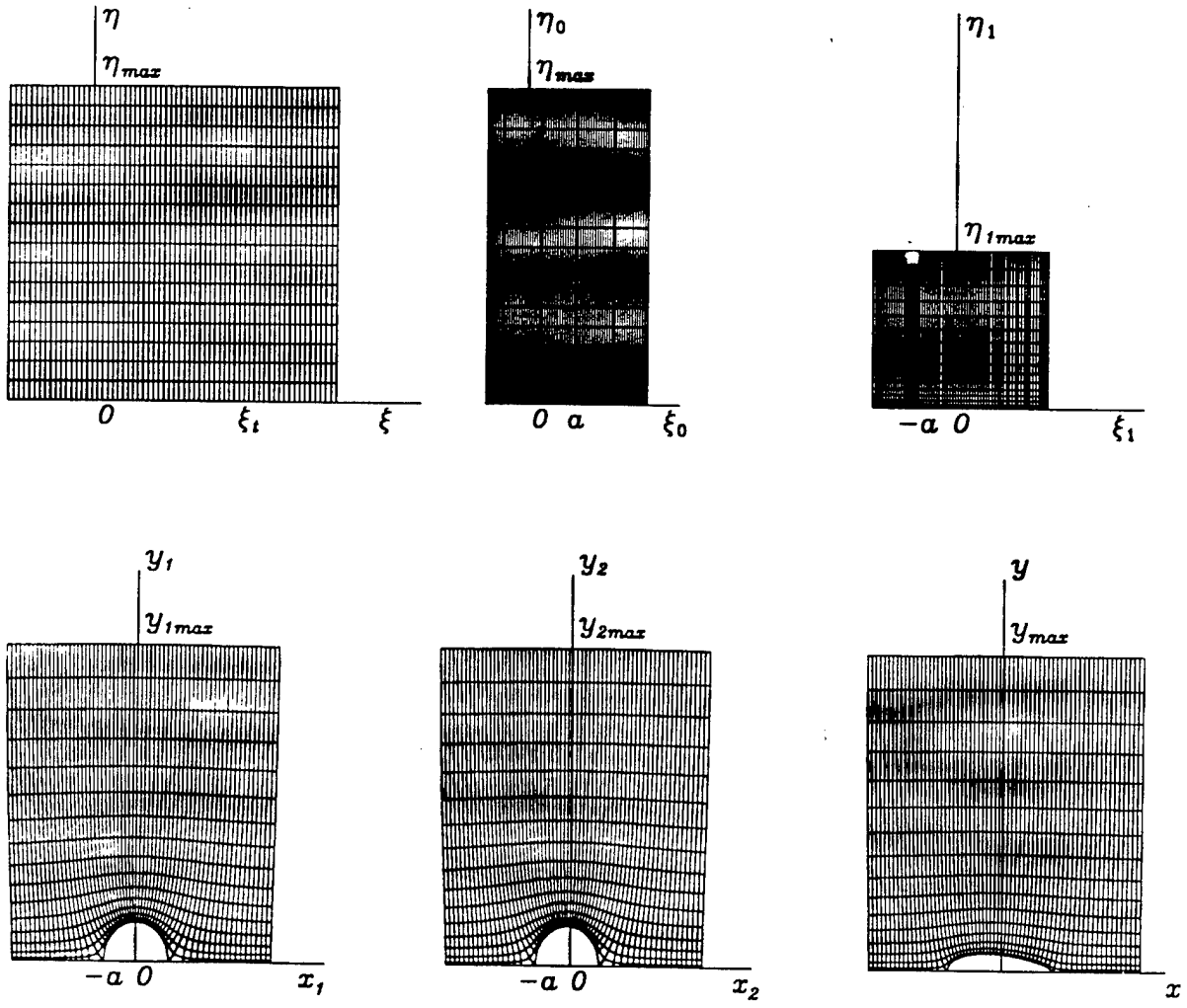

Figure 3. Conformal mapping process to obtain the grids for the Joukowsky airfoil.

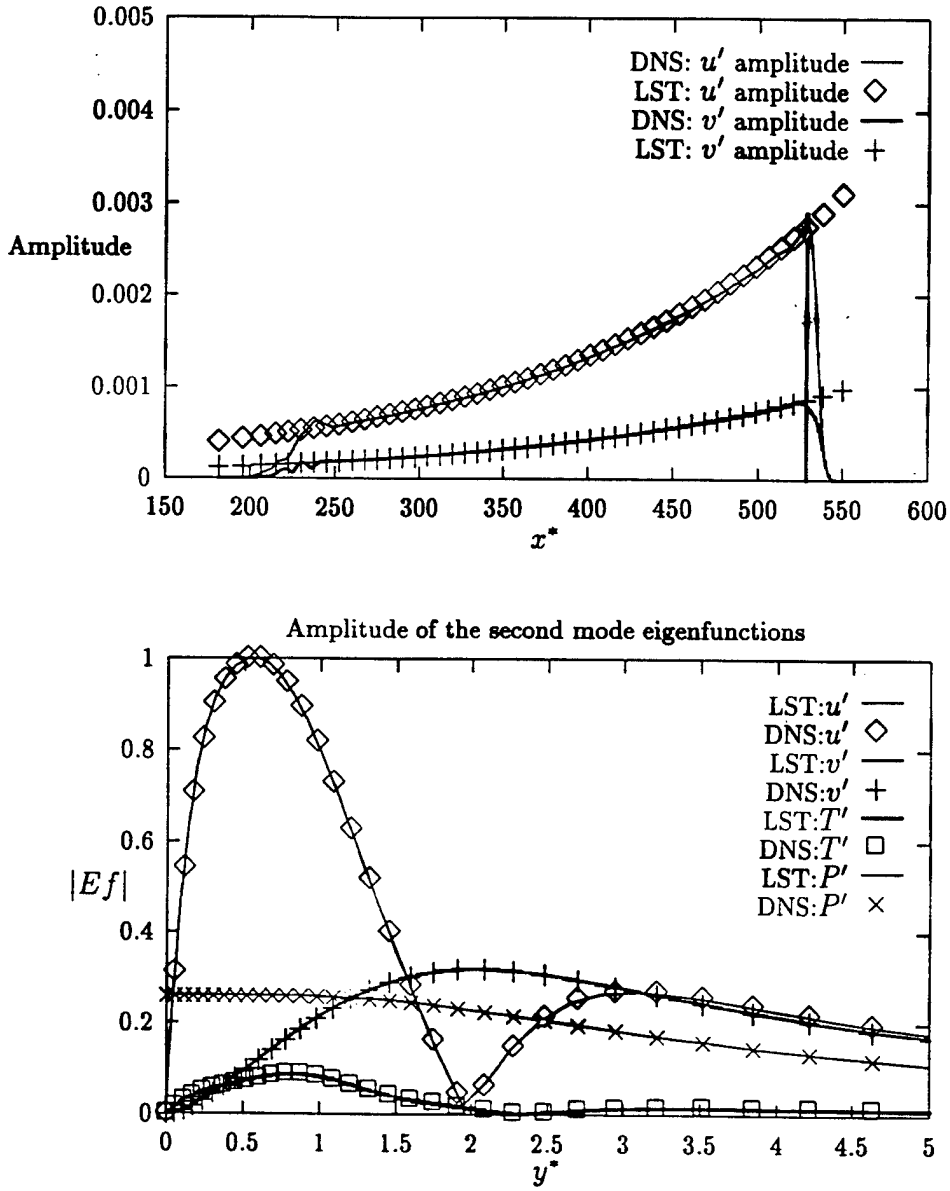

Figure 4. (a) Comparison between DNS and LST of the disturbance amplitude of the u' and v'. (b) Comparison of DNS and LST results for the amplitude eigenfunctions of subsonic flat plate boundary layer. $M_\infty = 0.5$, $Re^* = 875$, $\omega = 0.1$.

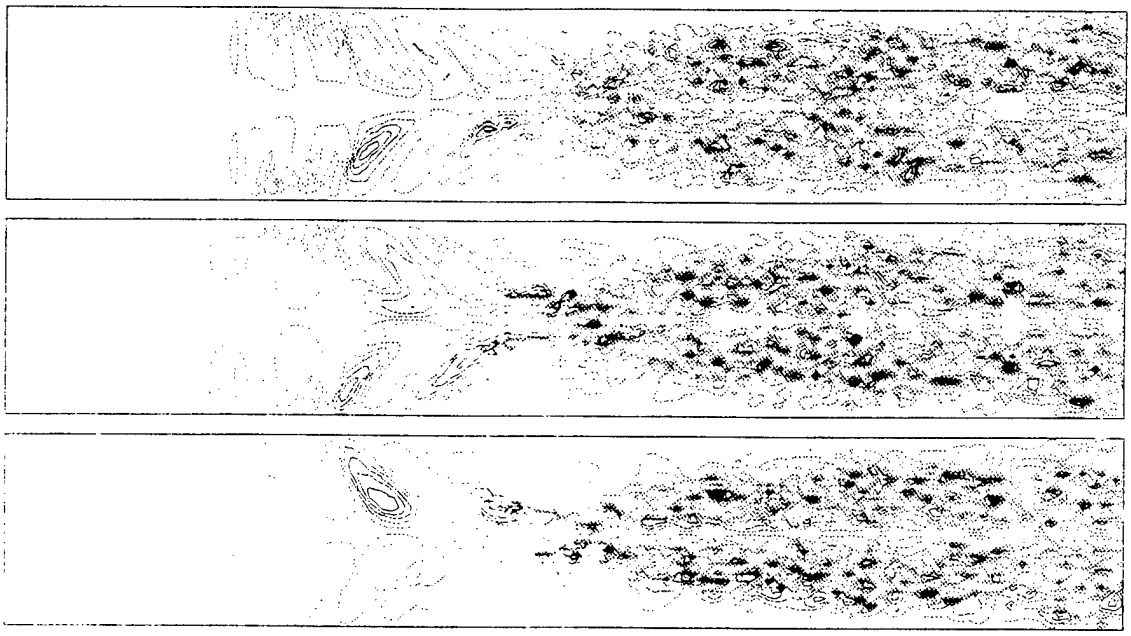

Figure 5. (a) Instantaneous contour plots of the streamwise perturbation vorticity ω_x on the $y^* = 0.18595,\ 0.48165,\ 0.85052$ (x, z) planes (from bottom to top) at $t = 10T$ for the flat plate fundamental breakdown case.

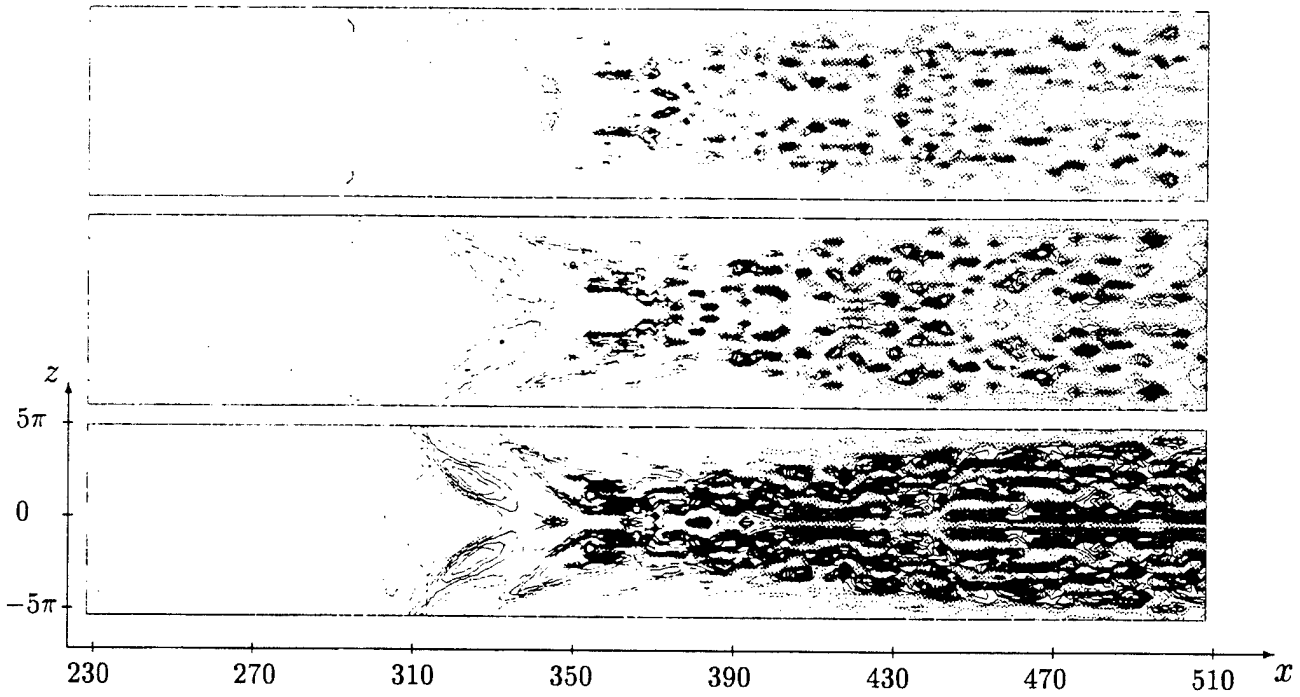

Figure 5. (b) Instantaneous contour plots of the spanwise perturbation vorticity ω_z on the $y^* = 0.18595,\ 0.48165,\ 0.85052$ (x, z) planes (from bottom to top) at $t = 10T$ for the flat plate fundamental breakdown case. Flow parameter: $M_\infty = 0.5$, $T_\infty = 288K$, $Re^* = 875$, $Pr = 0.72$, $\omega = 0.1$, $\varepsilon_{2d} = 0.02$, $\varepsilon_{3d} = 0.008$, $\beta = 0.2$. Grids: $193 \times 41 \times 32$.

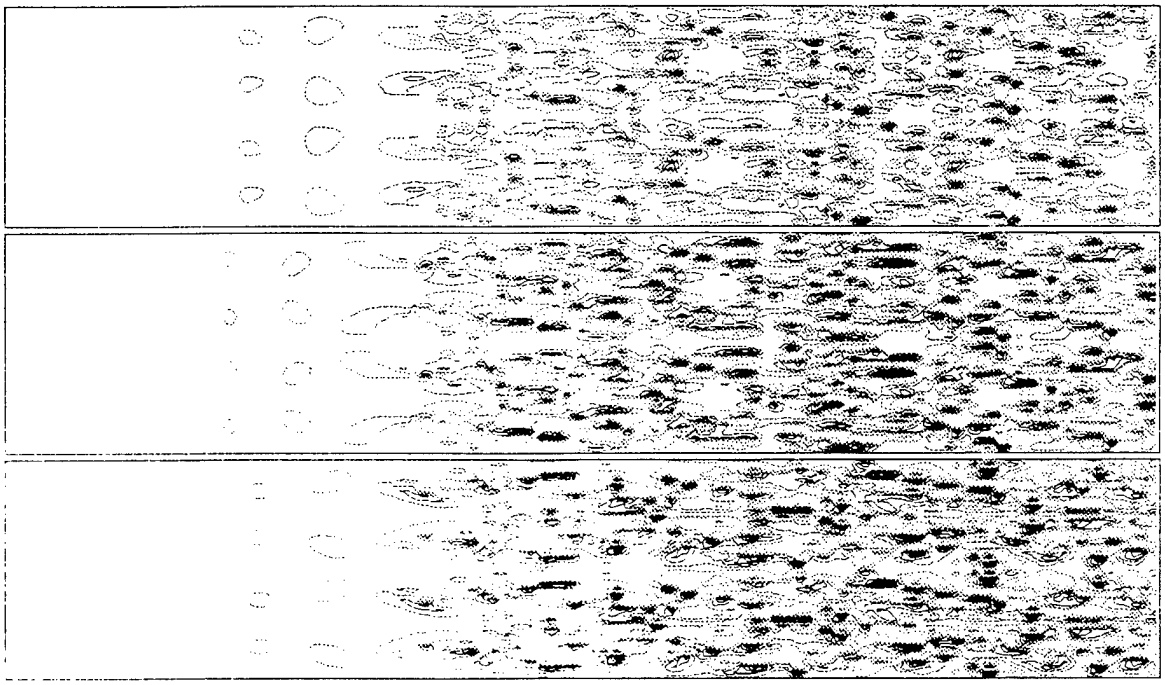

Figure 6. (a) Instantaneous contour plots of the streamwise perturbation vorticity ω_x on the $y^* = 0.1471, 0.3768, 0.6563$ (x, z) planes (from bottom to top) at $t = 11T$.

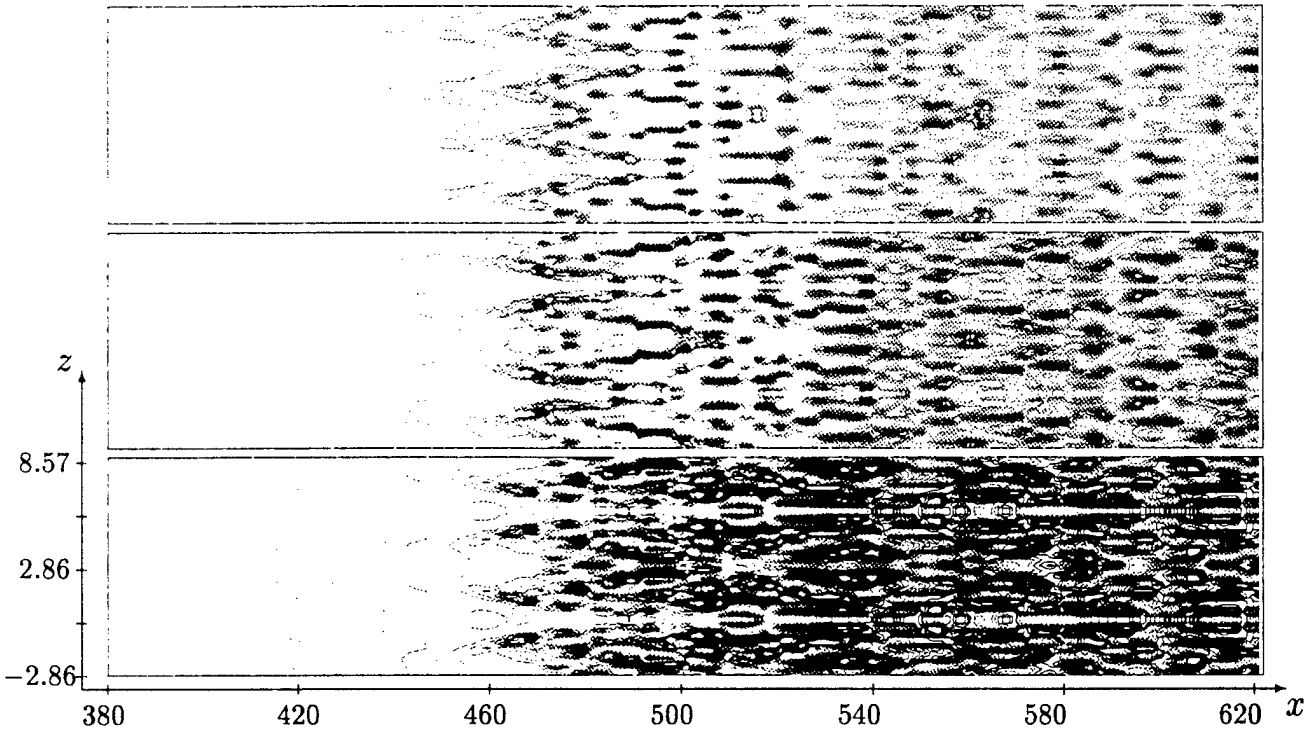

Figure 6. (b) Instantaneous contour plots of the spanwise perturbation vorticity ω_z on the $y^* = 0.1471,\ 0.3768,\ 0.6563$ (x, z) planes (from bottom to top) at $t = 11T$ for the flat plate subharmonic breakdown case. Flow parameter: $M_\infty = 0.8$, $T_\infty = 288K$, $Re = 1675$, $Pr = 0.72$, $\omega_{2d} = 0.15075$, $\varepsilon_{2d} = 0.012$, $\varepsilon_{3d} = 0.004$, $\beta = 0.22$. Grids: $265 \times 45 \times 42$.

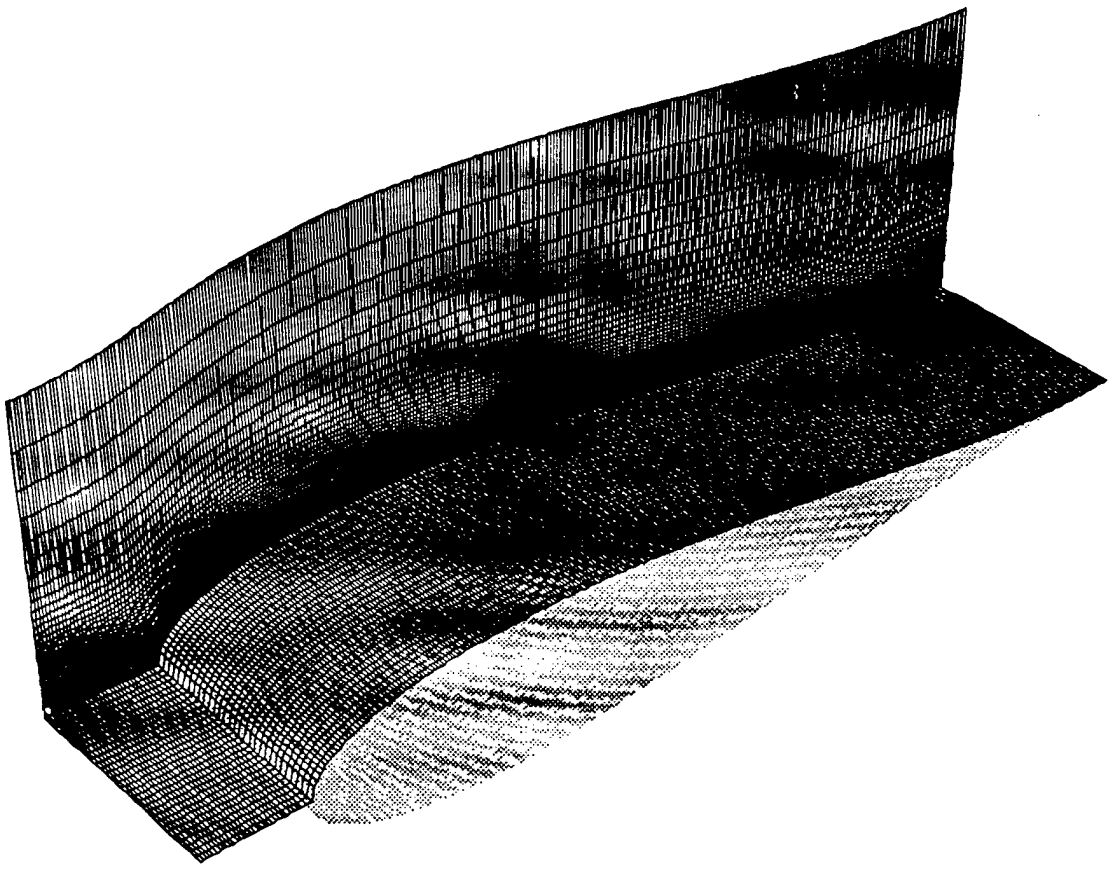

Figure 7. Grid structure for the subsonic Joukowsky airfoil transition simulation.

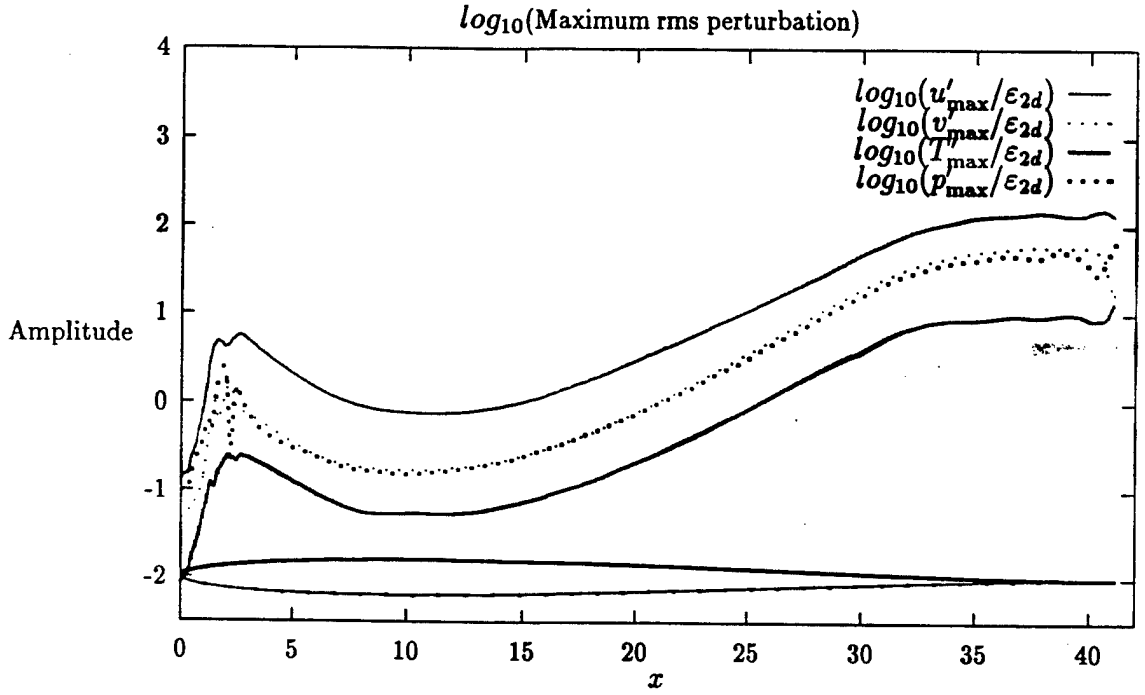

Figure 8. Streamwise distribution of the maximum perturbation rms amplitudes for the 2-D Mach 0.5 Joukowsky airfoil. $Re_h = 4000$, $\omega = 0.8$.

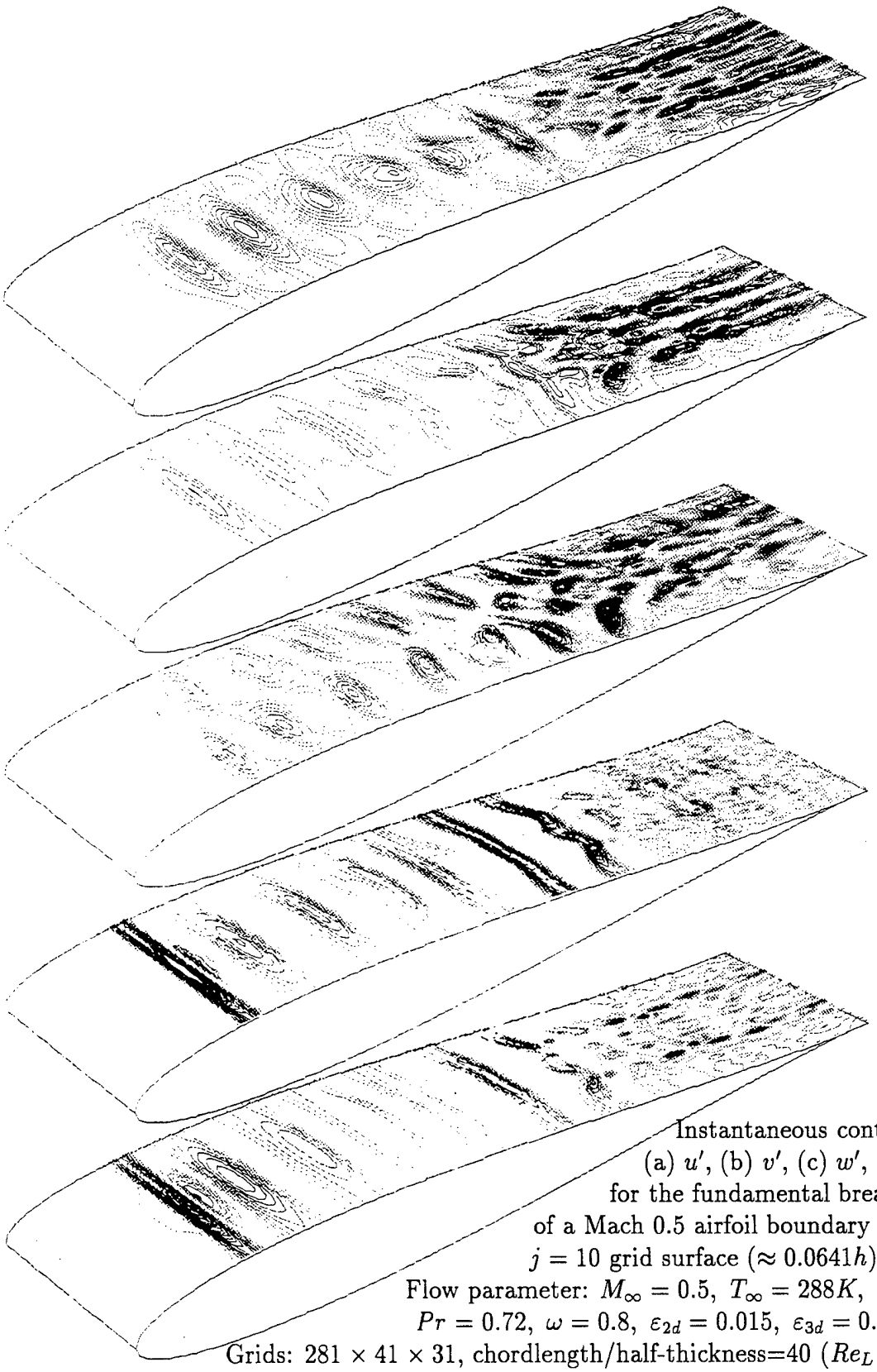

Figure 9.
Instantaneous contour plots of
(a) u', (b) v', (c) w', (d) p', (e) ρ'
for the fundamental breakdown case
of a Mach 0.5 airfoil boundary layer on the
$j = 10$ grid surface ($\approx 0.0641h$) at $t = 10T$.
Flow parameter: $M_\infty = 0.5$, $T_\infty = 288K$, $Re_h = 4000$,
$Pr = 0.72$, $\omega = 0.8$, $\varepsilon_{2d} = 0.015$, $\varepsilon_{3d} = 0.01$, $\beta = 1.3$.
Grids: $281 \times 41 \times 31$, chordlength/half-thickness=40 ($Re_L = 160,000$).

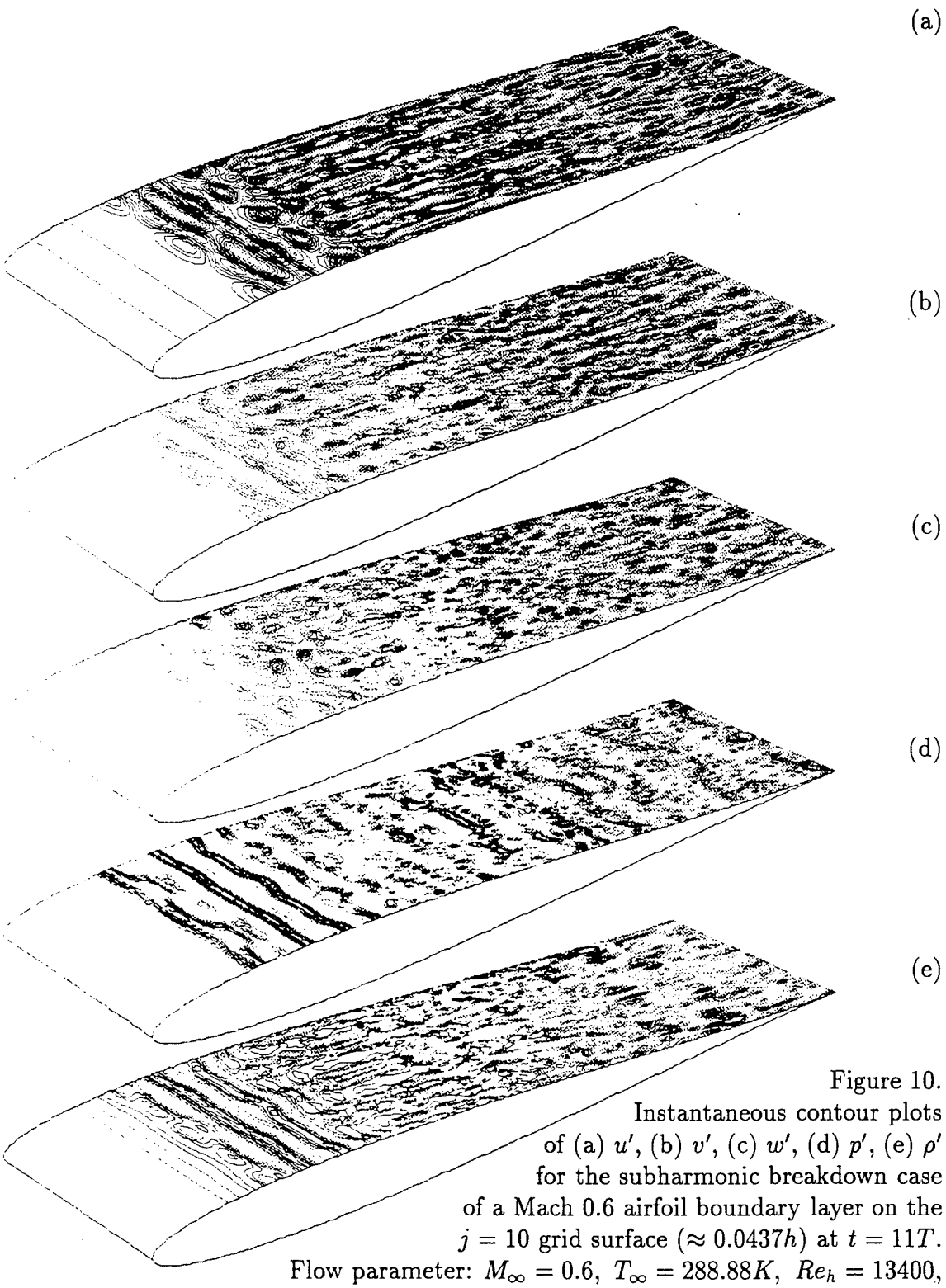

Figure 10.
Instantaneous contour plots
of (a) u', (b) v', (c) w', (d) p', (e) ρ'
for the subharmonic breakdown case
of a Mach 0.6 airfoil boundary layer on the
$j = 10$ grid surface ($\approx 0.0437h$) at $t = 11T$.
Flow parameter: $M_\infty = 0.6$, $T_\infty = 288.88K$, $Re_h = 13400$,
$Pr = 0.72$, $\omega = 1.206$, $\varepsilon_{2d} = 0.01$, $\varepsilon_{3d} = 0.0075$, $\beta = 1.76$.
Grids: $361 \times 45 \times 41$, chordlength/half-thickness=50 ($Re_L = 670,000$).

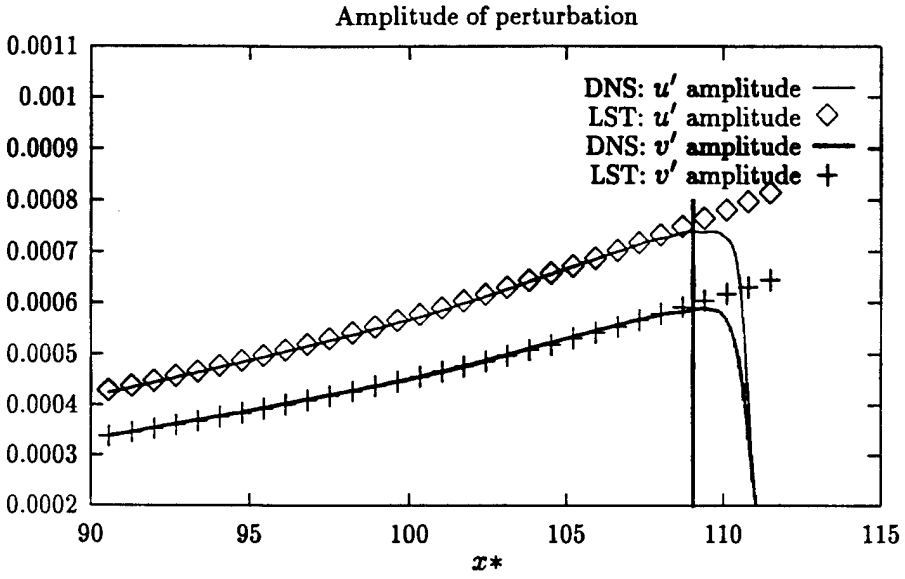

Figure 11. Comparison between DNS and LST of the disturbance amplitude of the second-mode disturbance u' and v' for Mach 4.5 flat plate boundary layer. $Re^* = 10,000$, $\omega = 2.0467$.

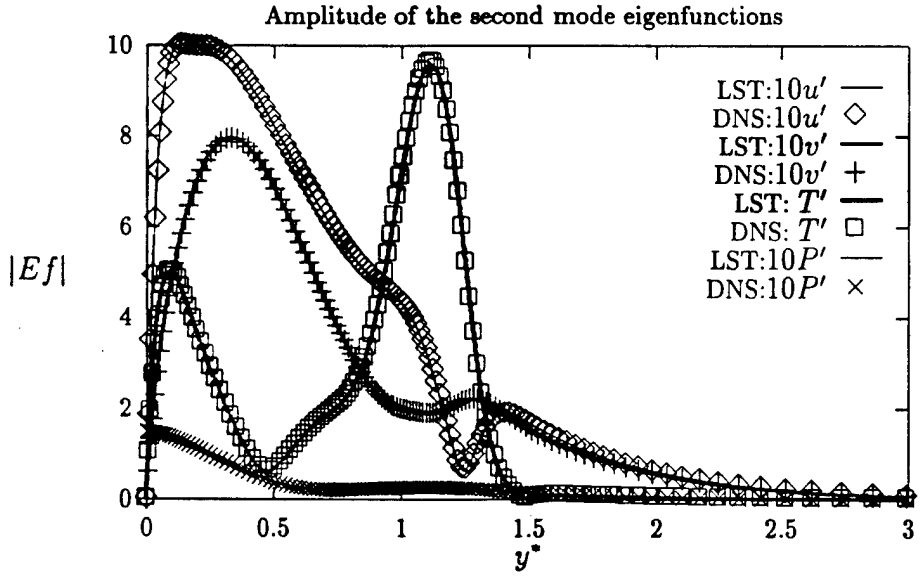

Figure 12. Amplitude eigenfunctions for supersonic flat plate transition: comparison of DNS and LST results for the second-mode disturbance at $M_\infty = 4.5$ and $Re^* = 10,000$.

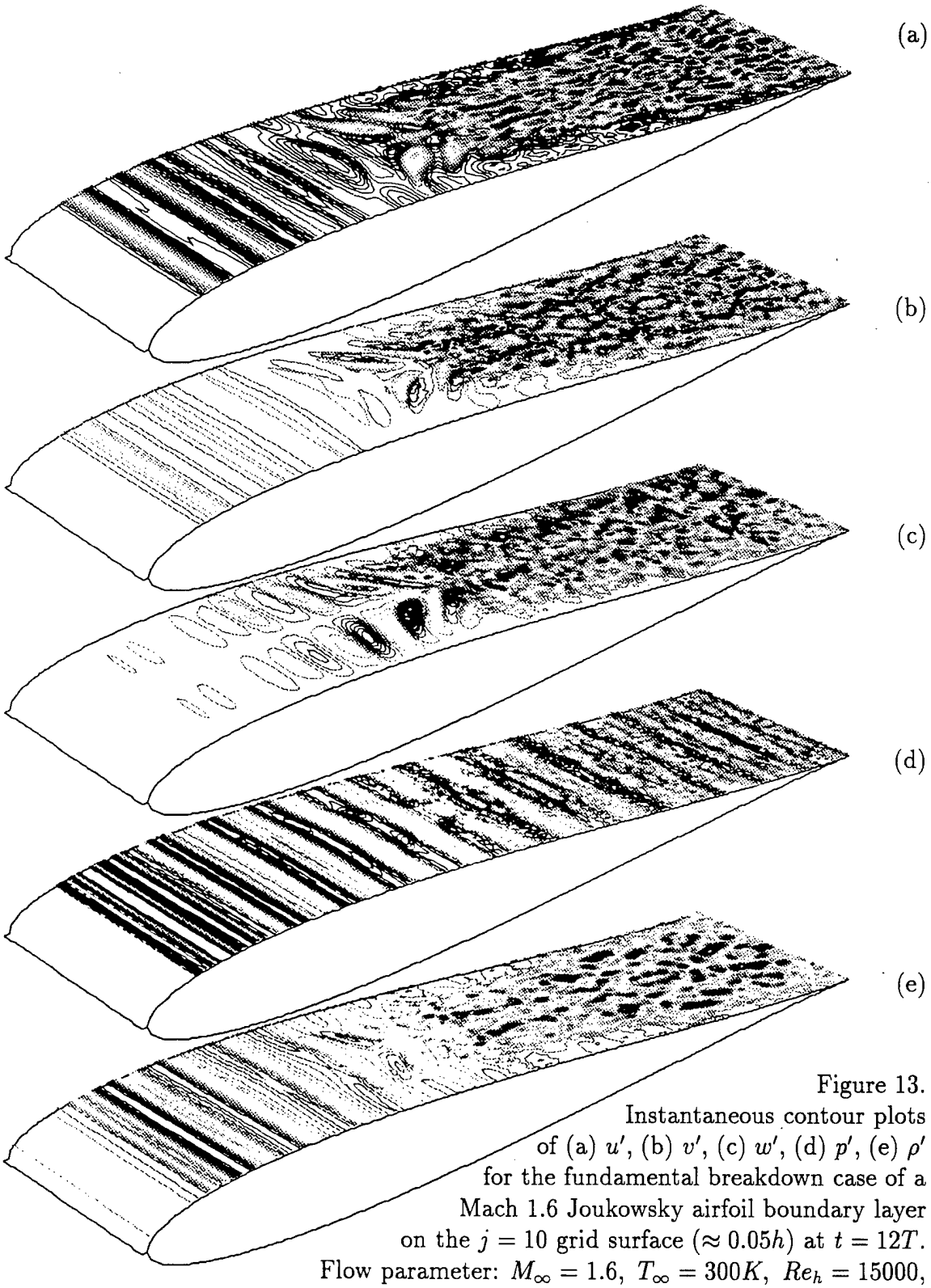

Figure 13.
Instantaneous contour plots
of (a) u', (b) v', (c) w', (d) p', (e) ρ'
for the fundamental breakdown case of a
Mach 1.6 Joukowsky airfoil boundary layer
on the $j = 10$ grid surface ($\approx 0.05h$) at $t = 12T$.
Flow parameter: $M_\infty = 1.6$, $T_\infty = 300K$, $Re_h = 15000$,
$Pr = 0.72$, $\omega = 0.75$, $\varepsilon_{2d} = 0.02$, $\varepsilon_{3d} = 0.001$, $\beta = 2.28$.
Grids: $361 \times 71 \times 37$, chordlength/half-thickness=60 ($Re_L = 900,000$).

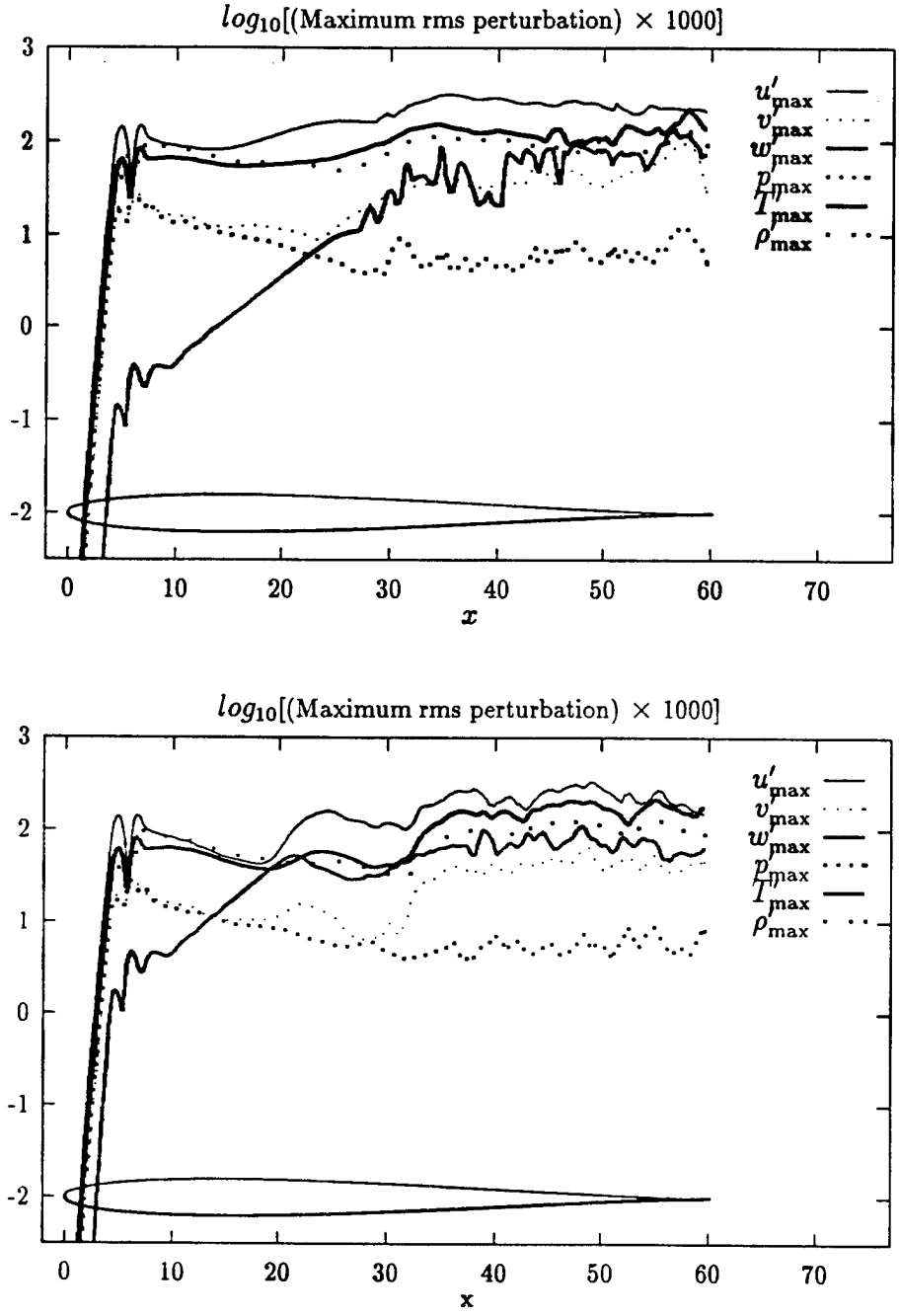

Figure 14. Streamwise distribution of the maximum rms disturbance for the fundamental breakdown case. $M_\infty = 1.6$, $F = 50 \times 10^{-6}$, and $Re_L = 900,000$. Upper: $z = 0.$, lower: $z = .0689$.

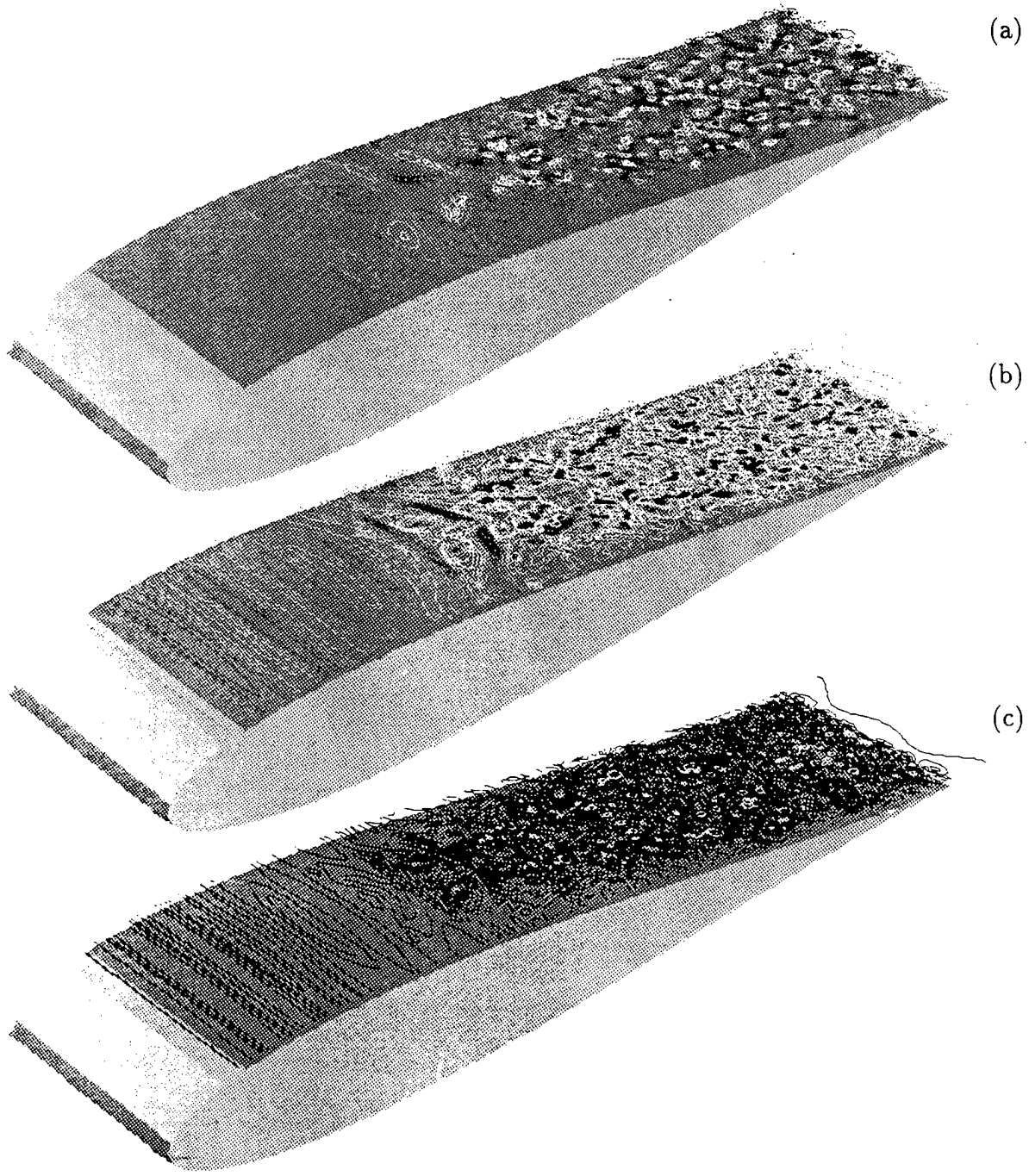

Figure 15. Instantaneous contour plots of (a) ω_x', (b) ω_z', (c) $|\omega'|$ for the fundamental breakdown case of a Mach 1.6 Joukowsky airfoil boundary layer on the $j = 20$ grid surface ($\approx 0.12h$ from wall) at $t = 12T$. Flow parameter: $M_\infty = 1.6$, $T_\infty = 300K$, $Re_h = 15000$, $Pr = 0.72$, $\omega = 0.75$, $\varepsilon_{2d} = 0.02$, $\varepsilon_{3d} = 0.001$, $\beta = 2.28$. Grids: $361 \times 71 \times 37$, chordlength/half-thickness=60 ($Re_L = 900,000$).

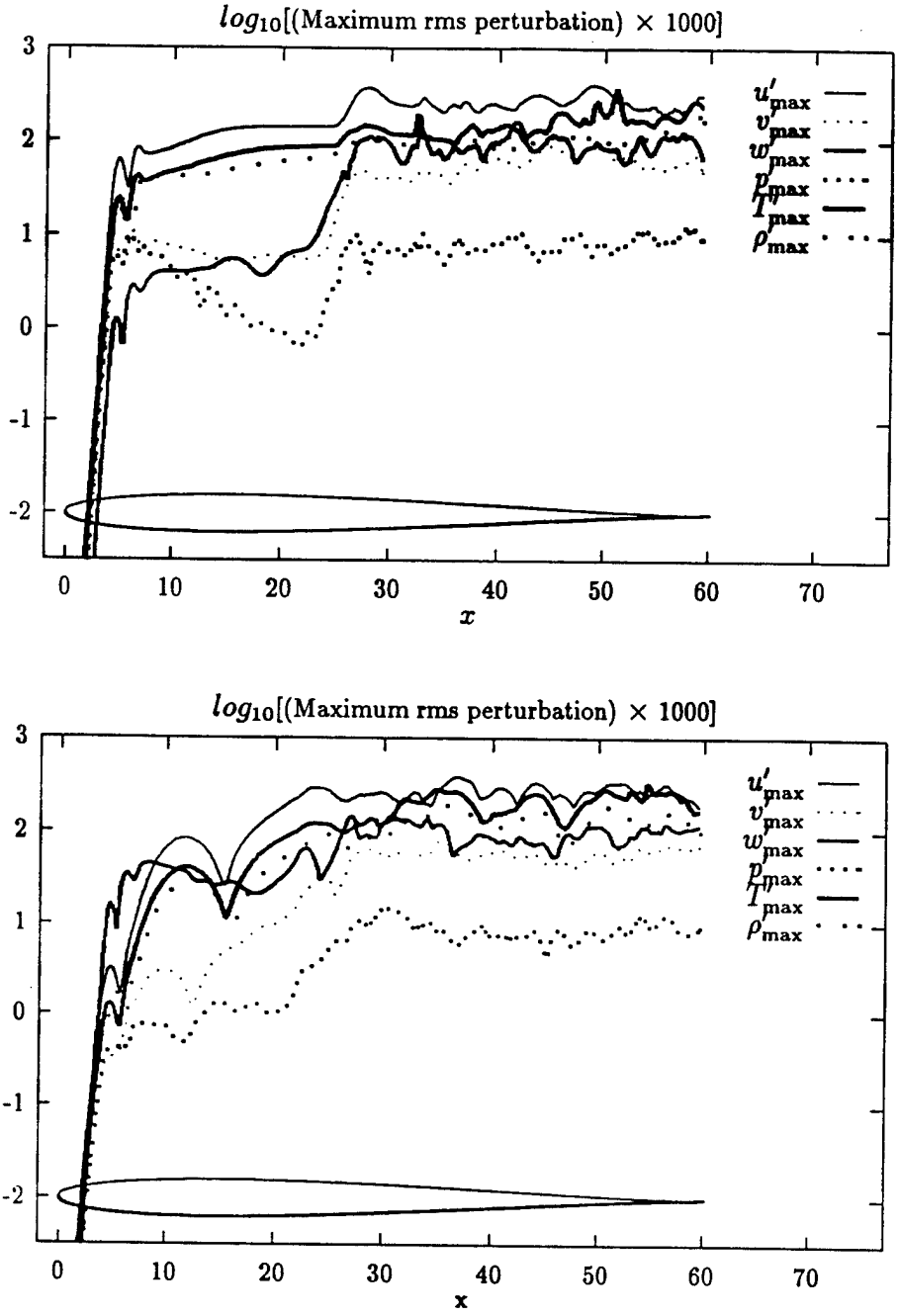

Figure 16. Streamwise distribution of the maximum rms disturbance for the oblique breakdown case. $M_\infty = 1.6$, $F = 50 \times 10^{-6}$, and $Re_L = 900,000$. Upper: $z = 0.$, lower: $z = 0.988$.

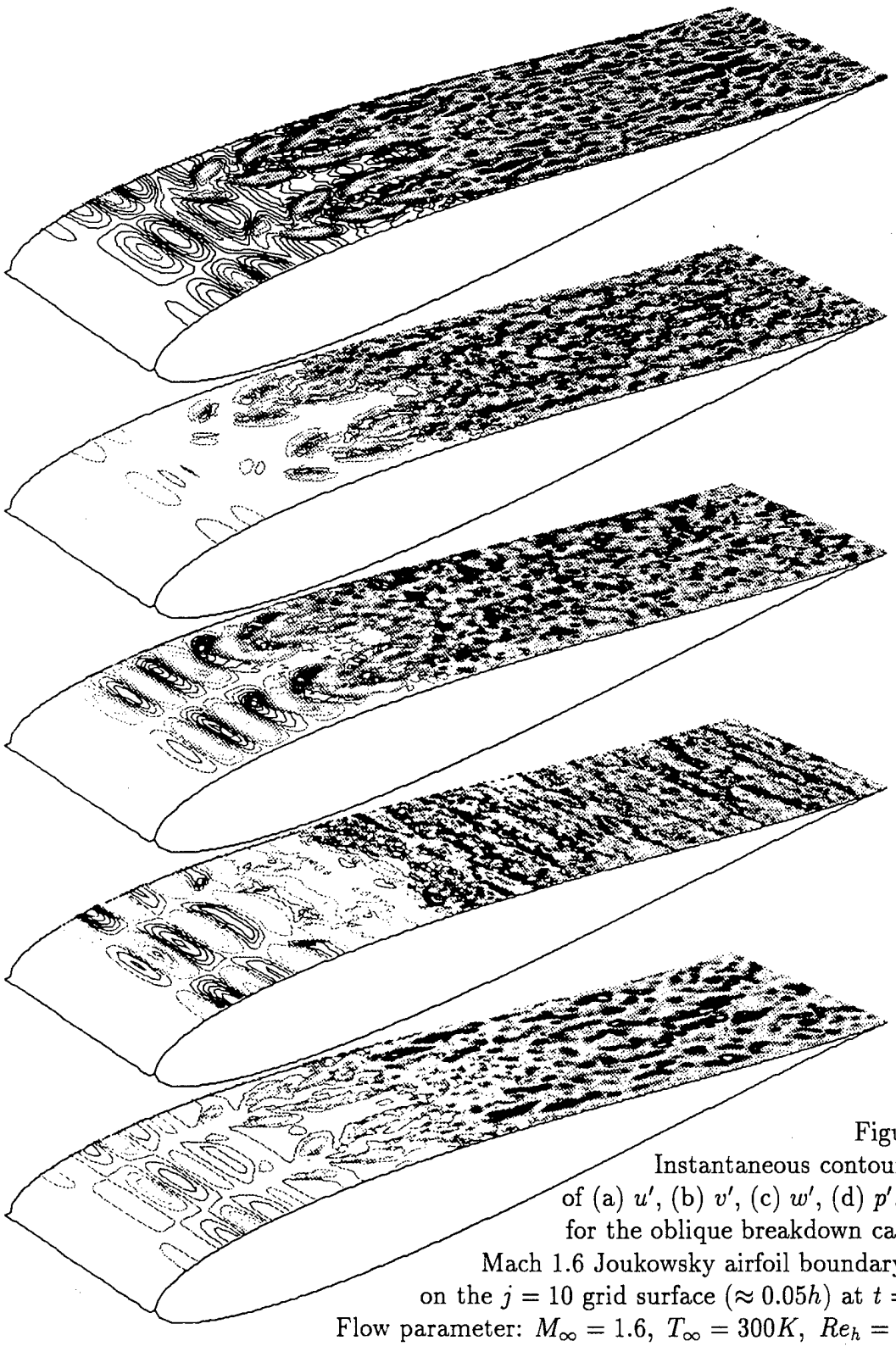

Figure 17.
Instantaneous contour plots
of (a) u', (b) v', (c) w', (d) p', (e) ρ'
for the oblique breakdown case of a
Mach 1.6 Joukowsky airfoil boundary layer
on the $j = 10$ grid surface ($\approx 0.05h$) at $t = 12T$.
Flow parameter: $M_\infty = 1.6$, $T_\infty = 300K$, $Re_h = 15000$,
$Pr = 0.72$, $\omega = 0.75$, $\varepsilon_{2d} = 0.0$, $\varepsilon_{3d} = 0.0075$, $\beta = 1.59$.
Grids: $361 \times 71 \times 37$, chordlength/half-thickness=60 ($Re_L = 900,000$).

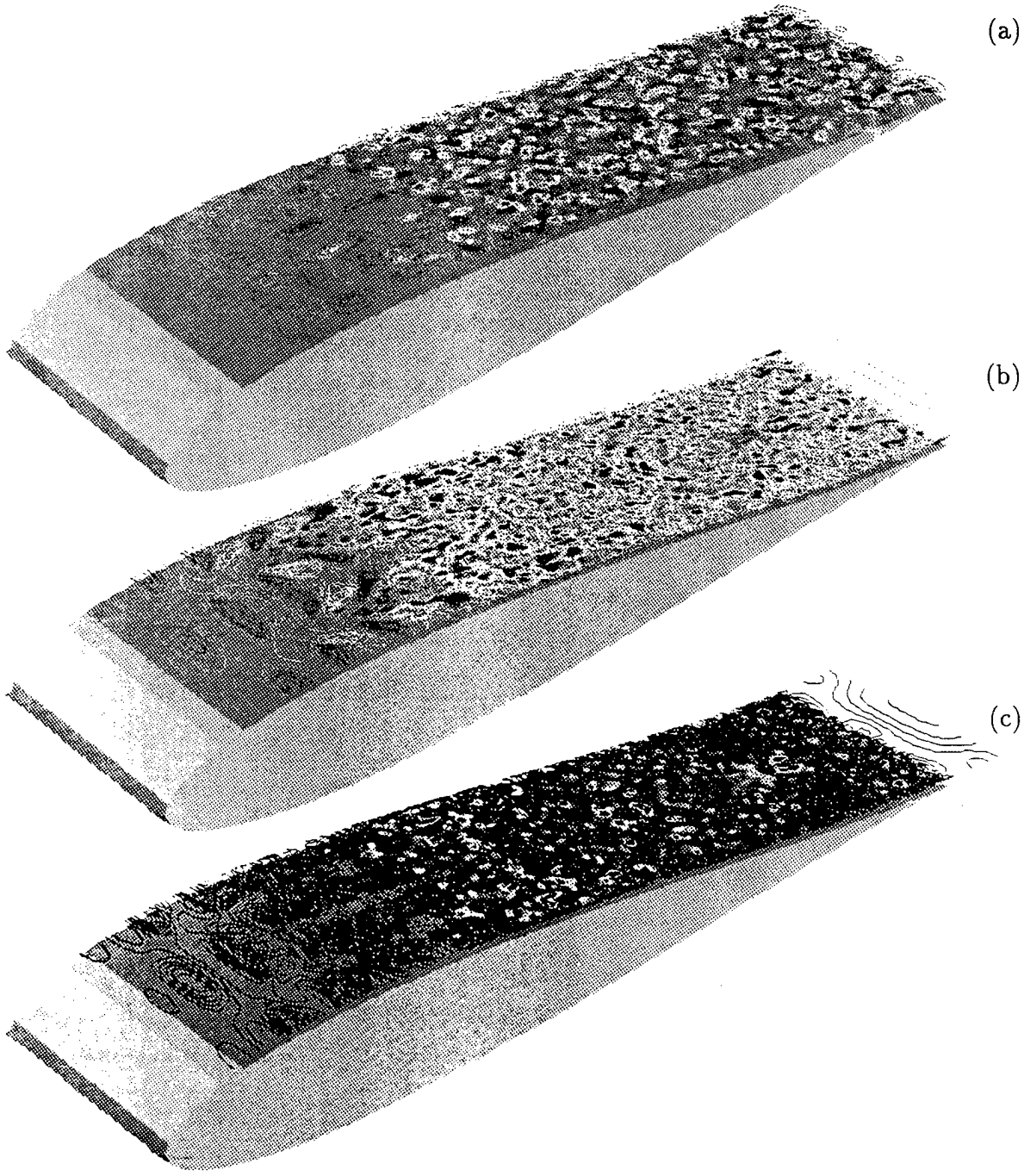

Figure 18. Instantaneous contour plots of (a) ω'_x, (b) ω'_z, (c) $|\omega'|$ for the oblique breakdown case of a Mach 1.6 Joukowsky airfoil boundary layer on the $j = 20$ grid surface ($\approx 0.1h$) at $t = 12T$. Flow parameter: $M_\infty = 1.6,\ T_\infty = 300K,\ Re_h = 15000, Pr = 0.72,\ \omega = 0.75,$ $\varepsilon_{2d} = 0.0,\ \varepsilon_{3d} = 0.0075,\ \beta = 1.59$. Grids: $361 \times 71 \times 37$, chordlength/half-thickness=60 ($Re_L = 900,000$).